Title
On the Development of Graphene Based Photonic Devices

Author
Pollack, Trevor McCall

Publication Date
2022

Peer reviewed|Thesis/dissertation

On the Development of Graphene Based Photonic Devices

By

TREVOR POLLACK
THESIS

Submitted in partial satisfaction of the requirements for the degree of

MASTER OF SCIENCE

in

Electrical and Computer Engineering

in the

OFFICE OF GRADUATE STUDIES

of the

UNIVERSITY OF CALIFORNIA

DAVIS

Approved:

Juan Sebastian Gomez Diaz, Chair

William Putnam

Erkin Seker

Committee in Charge

2022

Acknowledgements

I would like to thank my advisor, Professor Gomez Diaz, for his unrelenting dedication to my learning and success. I would also like to thank my parents, Kris and Dean, for giving me the support needed for my academic journey.

Abstract

Manipulation of terahertz (THz) waves provides an avenue for exploration and technological advancement because of their capability to interface with biological systems, imaging, security, space exploration, and sensing, as well as enabling ultra-fast communications (1000x current speeds). Unfortunately, this part of the electromagnetic spectrum is susceptible to substantial loss through the atmosphere, sizable enough to make it unusable over long distances in communication. However, over short distances (such as within the human body or on a chip) or in atmosphere-free conditions (such as space), THz can be capable of delivering unprecedented responses. The last decade has seen a surge in THz research for these applications due to advances in sources, detectors, and nanofabrication. Miniaturizing such systems is of importance because of their capability to be introduced into bioelectronic and microelectronic systems.

Graphene has been a material of interest since its experimental discovery in 2004 [1] because of its exceptional electronic, mechanical, and electromagnetic properties [2]. In addition, its compatibility with current CMOS (complementary metal oxide semiconductor) processes make it interesting to study using current semiconductor analysis techniques. Graphene's strong interaction with infrared and THz radiation make it a great candidate material for systems that exploit these regions of the electromagnetic spectrum. Its atomic thickness makes it appealing for the next generation of small scale electronics and its biocompatibility opens new doors for researchers in various fields of bioengineering to utilize this 2D material in their systems.

This thesis proposes and develops graphene-based devices that demonstrate state-of-the-art quality. These devices are then characterized electrically, optically, and at THz

frequencies. Methodology to further test these devices is proposed and future capabilities as well as potential application are described. This thesis starts by introducing the state of the art of THz and graphene technologies in Chapter 1. Chapter 2 introduces graphene's interesting electronic properties. Chapter 3 reports the fabrication of graphene-based devices, and Chapter 4 evaluates the quality of such devices. Chapter 5 subsequently reports the device's response to infrared (IR) light, and explores the influence of light polarization & intensity coupled with electronic stimulation. Chapter 6 reports the THz response and a methodology for determining the Faraday rotation in the THz spectrum. Chapter 7 finalizes the thesis and proposes how all of these fields of study can be combined to develop and implement novel graphene based devices that interact with the electromagnetic spectrum in innovative ways that would enable future research and exciting applications.

Chapter 1 - Introduction

Terahertz (THz) is a region of the electromagnetic spectrum whose frequencies lie between that of microwaves and infrared. THz waves propagate with .03 mm - 3 mm in wavelength (100 GHz - 10 THz). Interest in THz began to grow with the development of the Auston switch and ultrafast lasers in the 1970s [3]. However, suitable materials and techniques to generate and manipulate this part of the spectrum are far and few between, leading to the term dubbed in the scientific community “Tera-gap”. THz technologies that take advantage of existing materials and techniques have enabled new applications in the fields of sensing, imaging, spectroscopy, and high data-rate communications as well as a unique playground to investigate a wide variety of emerging physical systems such as graphene and 2D materials, topological configurations, and non-linear media. Recent improvements to THz sources and detectors have put a strain on researchers to develop miniaturized and efficient THz devices necessary to enable complete THz systems, including components such as circulators, isolators, polarizers, sensors, and filters. To enable such development, researchers are taking advantage of recent advances in materials science (graphene, 2D materials, phase-change materials) and nanophotonics (metamaterials composed of subwavelength resonators) to design nano-devices able to strongly interact with the THz spectrum and exhibit unprecedented functionalities. This thesis focuses on testing devices that take advantage of nonreciprocity to realize such capabilities.

Nonreciprocal devices are of critical importance in modern day communication technology. For instance, these devices are capable of allowing transmission in forward propagation with little loss, whereas little to no transmission can be found in backwards propagation. This is an important feature for the protection of sources and detectors from reflections, impedance matching, noise-canceling, and decoupling. Optical circulators, isolators

and directional amplifiers are examples of modern nonreciprocal devices. The most common nonreciprocal devices in the photonic regime are based on the Faraday effect [4], which rotates the polarization of the light with the help of magnetic materials. These magnetic materials are typically ferritic, making them bulky and thereby impossible to integrate in on-chip photonic designs. Therefore, it is of scientific interest to develop a miniaturized THz Faraday rotator that does not require the use of magnets and can achieve a high degree of rotation.

Faraday rotation was first demonstrated in a two dimensional material with a 2-D electron gas [5]. There are now multiple demonstrations of Faraday rotation at THz through graphene [6],[7] . The Faraday rotations demonstrated in these experiments were impressive, but required a large magnetic field (~7 T) and produced a rotation too small (~6 degrees) to be usable in an isolator device where 45 degrees of rotation is usually needed. Similar results have been found with Weyl semimetals at room temperature [8]. THz isolators have recently been developed using various materials such as yttrium iron garnet (YIG) [9], or InSb [10] but they all require an external magnetic field and some even require a bulk material [11], [12] . A small THz Faraday rotation (.45 degrees) has been demonstrated with topological insulator materials without an external magnetic field, however the devices were not capable of demonstrating a rotation at room temperature and needed to be cooled down to 1.5 K [13].

There have been methods proposed, such as strain engineering, to enhance the local magnetic field within the graphene to produce a large Faraday effect usable in isolator devices [14]. Additionally, it has been theorized that circularly polarized light can act to “magnetize” graphene, effectively acting as the magnetic field needed for Faraday rotation [15]. When these two phenomena are simultaneously impressed upon high quality graphene, it is theoretically possible to enable a magnetless THz Faraday rotation in a two dimensional material large enough

to realize isolation. This thesis aims to develop devices capable of such an impressive feat, and characterize such devices' response to optical polarization & intensity; as well as THz and electrical stimulation.

Chapter 2 - Graphene

Graphene is a new 21st century material of interest because of its remarkable optical, electrical, mechanical, and chemical properties and its 2D structure. Graphene is a hexagonal lattice of carbon atoms, arranged in a layer one atom thick. Graphene has an unusual dispersion relation that leads to effectively massless electrons, otherwise known as Dirac fermions, that travel at a constant speed known as the Fermi velocity, $v_F = 10^6 m/s$ [16]. This phenomenon can be approximately described by the following equation:

$$E(k) \approx \pm \hbar v_F |k| \quad (1)$$

where *E* and *k* are the electron energy and momentum, and ħ is the reduced Planck constant. Each carbon atom in the graphene lattice has four electrons, three of which are tied up in bonds. This leaves one electron that is essentially free and can travel great distances (compared to semiconductors) without collisions, i.e, it can travel ballistically. These charge carriers are capable of exhibiting ballistic current in exfoliated "pristine" graphene [17] and recently in chemical vapor deposition "lower-quality" graphene [18], [19]. Additionally, the charge carrier density in graphene can be controlled by applying a gate voltage to an integrated gated device. This changes the Fermi level and thus, the conductivity of graphene. Graphene has a theoretical minimum conductivity $\frac{4q^2}{h}$ (~155 μS) when there are absolutely no carriers present [2]. This is practically difficult to achieve because of the impurities that present themselves during the fabrication process. However, even if the impurities cannot be removed from graphene, it is still a very interesting candidate for next generation electronic devices. The carriers can move up to 100 times faster than modern semiconductor devices, and graphene's conductivity can be

modulated in a similar fashion to modern day semiconductor electronics. This is important in electronics because this means that, in transistor terms, graphene based devices can turn on and off 100 times faster than conventional silicon (Si) devices. This phenomenon is manifested through the commonly used metric known as carrier mobility. Graphene has been shown to have a carrier mobility of $200,000\ cm^2V^{-1}s^{-1}$ whereas Si has a carrier mobility of $1,400\ cm^2V^{-1}s^{-1}$ and InSb (indium antimonide), the highest mobility semiconductor known has a carrier mobility of $77,000\ cm^2V^{-1}s^{-1}$. It should be mentioned that this analogy is presented solely to make a comparison of electronic quality and not to suggest that graphene can be readily applied to construct practical transistors because of the current on - current off ratio.

Aside from exciting electronic capabilities, graphene is also capable of demonstrating very interesting optical phenomena. Graphene absorbs 2.3% of all visible light that it interacts with, giving it the highest optical absorption per thickness known [20]. Graphene is capable of broadband, saturable [21], and tunable [22] optical absorption, as well as polarization dependent phenomena. Graphene exhibits a constant optical conductance of $G_0 = \frac{q^2}{4\hbar}$ [23] at visible frequencies. In ultrafast optical experiments, two distinct timescales appeared that reveal the carrier dynamics. On the ~100 fs timescale, intraband dynamics are observable and are associated with carrier-carrier scattering and phonon emission. On the ~ps timescale, interband dynamics are observable, associated with interband relaxation and cooling of hot phonons. Graphene was shown to demonstrate an unusual quantum hall effect, which manifested itself in the form of off-diagonal conductivity [24].

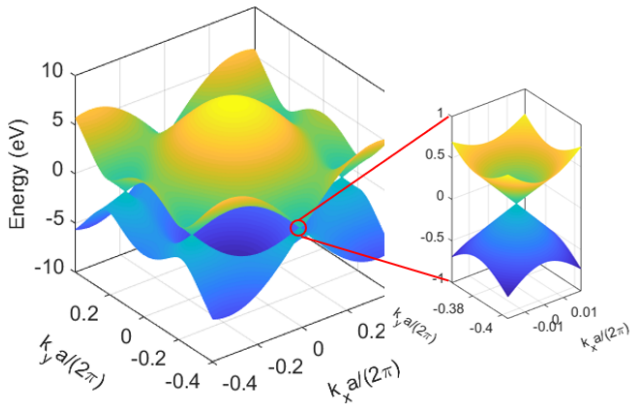

Figure 1 : The dispersion relation of graphene and the band structure around the Dirac point.

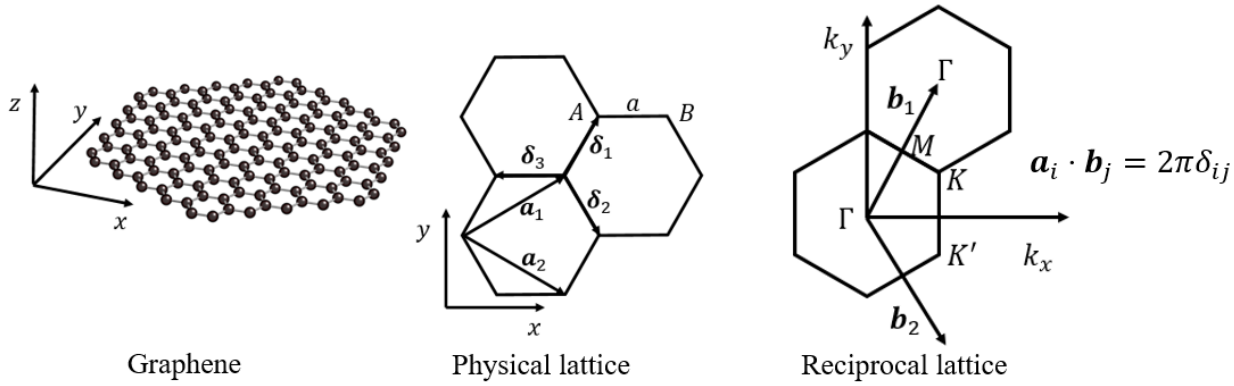

Figure 2 : The lattice structure of graphene.

Implementing the nonreciprocal effects that break time-reversal symmetry with graphene requires that the graphene is magnetized, usually with a strong magnetic field on the order of a few Tesla. A graphene sheet in the xy plane with a perpendicular magnetic field in the z direction will exhibit a gyrotropic response that can be expressed in tensorial form as:

$$\sigma_g = \begin{bmatrix} \sigma_{xx} & \sigma_{xy} \\ \sigma_{yx} & \sigma_{yy} \end{bmatrix} = \begin{bmatrix} \sigma_d & \sigma_o \\ -\sigma_o & \sigma_d \end{bmatrix} \tag{2}$$

Both σ_o and σ_d are complicated expressions that take into account all possible interband and intraband transitions between quantized energy levels in the graphene band diagram in the

presence of a static magnetic field [25]. However, if the graphene is heavily doped, these expressions can be simplified at THz and far-IR frequency into a Drude model [26]:

$$\sigma_0 = ne\mu \tag{3}$$

$$\sigma_d = \sigma_0 \frac{1 + j\omega\tau}{(\omega_c\tau)^2 + (1 + j\omega\tau)^2} \tag{4}$$

$$\sigma_o = \sigma_0 \frac{\omega_c\tau}{(\omega_c\tau)^2 + (1 + j\omega\tau)^2} \tag{5}$$

$$\omega_c = \frac{eB_0 v_F^2}{\mu_c} \tag{6}$$

where σ_0 is the DC conductivity, n is the carrier concentration, μ is the carrier mobility, σ_d is the diagonal conductivity, σ_o is the off diagonal (Hall) conductivity, τ is the relaxation time, ω_c is the cyclotron frequency, B_0 is the applied magnetic field, v_F is the Fermi velocity, and μ_c is the chemical potential. In the Drude model, the carrier concentration and carrier mobility can be approximately calculated as follows:

$$n = \frac{\mu_c^2}{\pi\hbar^2 v_F^2} \tag{7}$$

$$\mu = \frac{e\tau v_F^2}{\mu_c} \tag{8}$$

where μ_c is the chemical potential. It can then be seen that increasing the number of carriers should increase the chemical potential and decrease the mobility. Additionally, the recombination time increases with mobility. Using a carrier mobility of $5000\ \frac{cm^2}{Vs}$ at a carrier concentration of $2x10^{12}\frac{1}{cm^2}$, leading to a carrier lifetime of 83 fs, the plot shown in Fig. 3 can be generated for a

magnetic field of 1 Tesla. As can be seen from Figure 3, the most interesting behavior in the conductivity happens in the THz region above the cyclotron frequency (gray line). The quality of graphene simulated in this model is nearly identical to the quality of the graphene fabricated for this thesis.

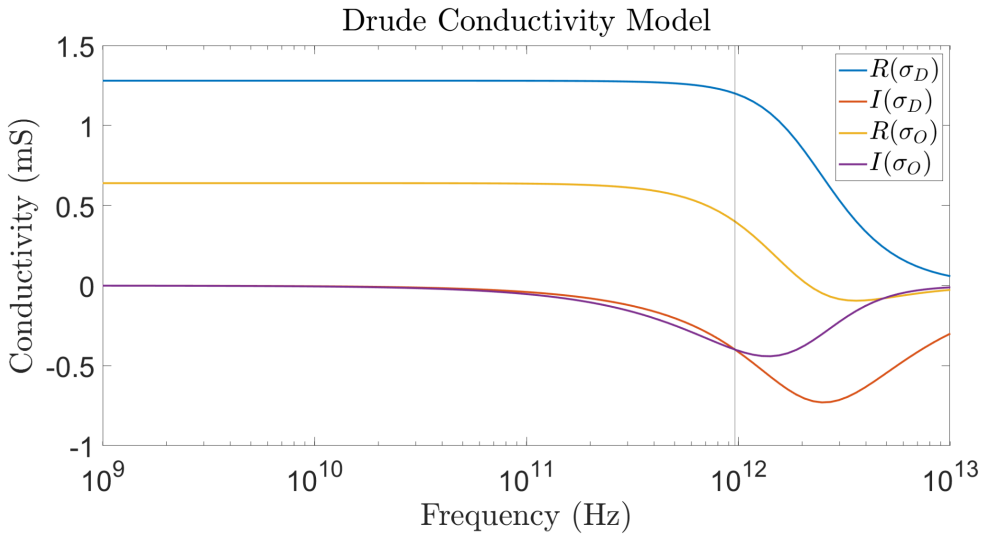

Figure 3 : Graphene's real ($R(\sigma_D)$ & $R(\sigma_0)$) and imaginary ($I(\sigma_D)$ & $I(\sigma_0)$) AC conductivity that shows interesting behavior beyond the cyclotron frequency (gray line).

Chapter 3 - Fabrication of Samples

A significant effort has been made over the last decade to improve the fabrication of graphene. There are currently three main methods to achieve its synthesis: mechanical cleavage (MC), epitaxial growth (EG) , and chemical vapor deposition (CVD). The MC technique was first demonstrated in 2004 by repeatedly ripping pencil lead apart with the aid of Scotch tape [1]. This technique produces the highest quality graphene, however the size of each flake (often only a few μms) and the time to produce each flake limits the process to research scale as opposed to industrial scale. The EG technique was first demonstrated in 2006 by heating a silicon carbide (SiC) wafer at 1000 °C to evaporate all silicon from the surface and to generate a layer of graphite [27]. It is difficult to generate single layer graphene in this manner and the process is costly. Oftentimes multilayer graphene is generated and the SiC wafers are on average 30 times as costly as silicon. The final technique is CVD, where carbon atoms are decomposed from a hydrocarbon (such as methane) and are nucleated as a single layer on a surface (such as copper) [28]. The advantages of using CVD graphene are that devices can be made to almost an arbitrary size, exhibit similar quality, and be made in a cost effective and scalable manner. For these reasons it is believed that CVD graphene *currently* has the most potential to be implemented into actual devices that interact with the electromagnetic spectrum.

The goal of this fabrication process is to develop a chip that acts as a substrate and testbed for high quality graphene. The end goal is to successfully test a four terminal hall effect device for the measurement of both diagonal and off diagonal conductivity in graphene at DC, infrared, and THz. The following section describes the incremental advances made towards achieving this goal and the detailed process that was implemented.

To isolate CVD graphene such that it can be transferred to a target substrate, the wet transfer process was used originally described in reference [59]. The wet transfer process is described in additional detail in many of the experiments referenced in this thesis [21,30,37,38,41,54,55,56]. The process starts with premade CVD graphene grown on both sides of copper foil using a method found in references [18,19, 28]. The CVD process consists of injecting methane gas into an ambiently heated reaction chamber with cleaned, heated copper foil as the substrate for the graphene growth [58]. The premade graphene/copper foil is cut with scissors to the desired size and the copper flake is taped to plastic printer film using single sided Kapton tape with a window left in the middle. The flake is then spin coated with PMMA (poly-methyl methacrylate) at 3000 rpm for 1 minute. The flake is then baked at 90 °C for 3 minutes. The flake is then cut out, flipped over, and taped to another piece of plastic film. The flake is etched in oxygen plasma to remove the graphene from the backside. The flake is then cut out of the tape and plastic and placed PMMA side up in .2 M ammonium persulfate until the copper is completely etched (~1 hour). The PMMA/graphene structure is scooped from the etching solution and transferred to deionized (DI) water to rinse for 30 minutes. The rinse process is repeated once more. Finally, the PMMA/graphene structure can then be scooped out with the target substrate (silicon dioxide on silicon - SiO_2/Si) The process is illustrated in Figure 4.

The fabrication of 4 terminal graphene devices for Hall effect measurements requires 4 electrodes directly in contact with graphene (source/drain) and an electrode that contacts the doped silicon under the oxide layer (gate) to change the chemical potential or Fermi level of the graphene. To create such a device, a photomask is used to i) deposit alignment marks, ii) etch the oxide and deposit the gate, iii) deposit the source/drain electrodes, iv) define the active area of

the graphene. Additionally, there is a 4 electrode transmission line structure on the device for measuring the contact resistance of the device. The contact resistance was not studied in this thesis, as the resolution of the lithography tool could not capture the structure, nor does our current method involve patterning the graphene, the reasons for which are discussed in the following paragraphs. Figure 5 shows a cross section of the device and Figure 6 shows a microscope image of the first version of devices that were fabricated.

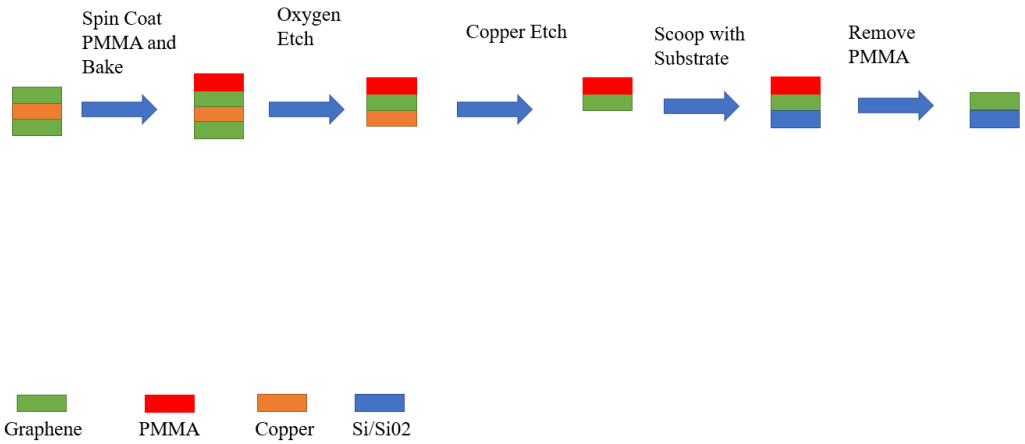

Figure 4: The fabrication process for a graphene/SiO_2 device with an impregnated gate electrode.

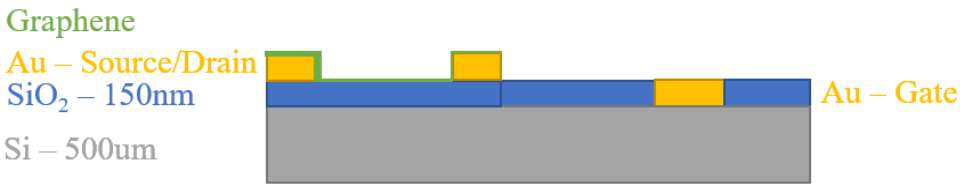

Figure 5: Cross section view of a graphene/SiO_2 device with an impregnated gate electrode.

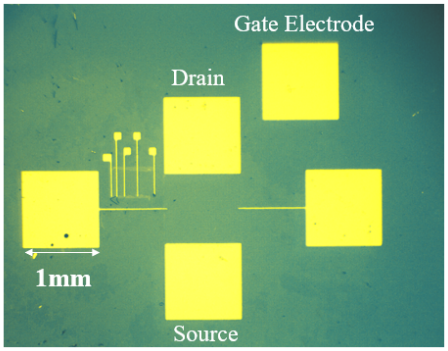

Figure 6 : Top view of graphene/SiO_2 device with an impregnated gate electrode.

An overlooked detail in this first design was the fact that the gate electrode was impregnated within the silicon dioxide. This effectively lowers the breakdown voltage of the oxide, which is normally 2.7 V/nm [29]. Theoretically, the device should be able to handle 405 V of gate voltage before breaking down, but the devices fabricated with this design could typically only handle 10-40 V before breaking down. The devices break because the oxide breaks down at relatively low voltages. A figure of the breakdown process is illustrated below. The gate current should be approximately zero versus gate voltage, which is the case until the gate voltage reaches around 28 V, at which point the gate oxide begins to break down. The breakdown process is completed when the gate voltage reaches 38 V. When the same device is tested for a second time, it is clear that the gate oxide is conducting current, as shown in Figure 7. The effects of gate oxide breakdown can be seen even more clearly with the $I_d - V_g$ plot as shown in Figure 8. The figure shows the gate breaking down completely at 38 V of applied gate voltage. When the test is run again, the drain current is unable to exhibit the proper behavior versus the gate voltage.

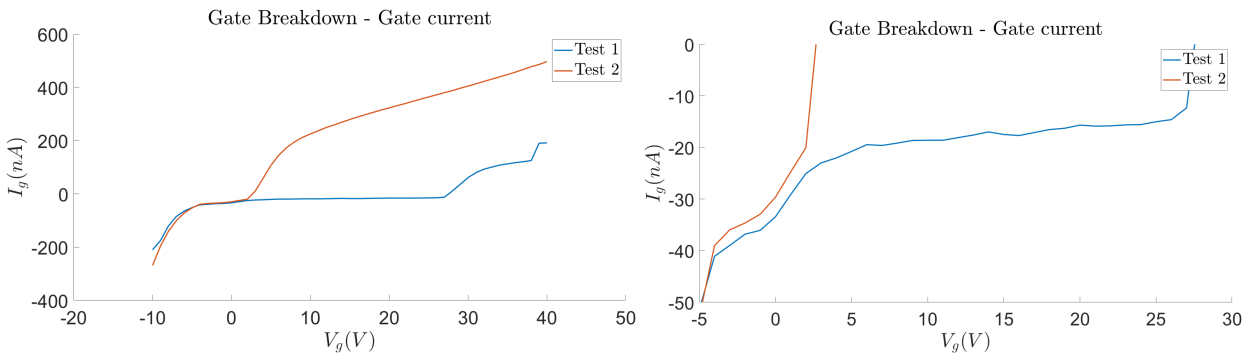

Figure 7 : Gate current vs gate voltage for a graphene/SiO_2 device with an impregnated gate electrode showing the first sweep (gate oxide breakdown around 28 V) and the second sweep (gate oxide has broken down already).

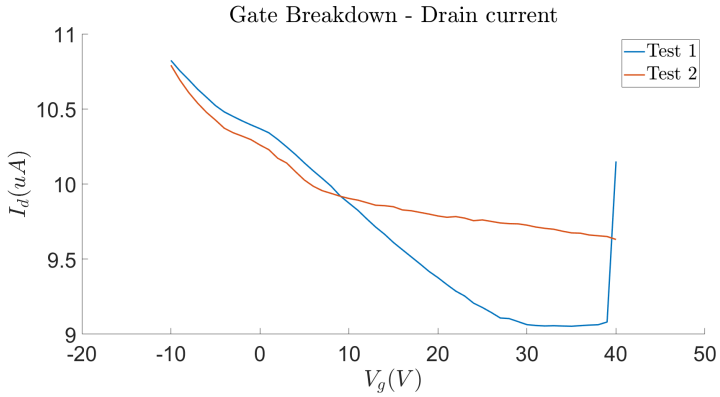

Figure 8 : Drain current vs gate voltage for a graphene/SiO_2 device with an impregnated gate electrode showing the first sweep (gate oxide breakdown around 28 V) and the second sweep (gate oxide has broken down already).

A solution to this problem was realized after reviewing previous works on back-gated graphene devices where the gate is not impregnated within the oxide [30]. This was implemented by using the same source/drain electrode mask as before, covering the source/drain electrodes in paper for protection, and then using Kapton tape to act as a hard mask. The wafer was etched via RIE to expose the silicon. Another layer of tape was applied to act as a second hard mask for the

gate electrode. The result was gold deposition only on the silicon with about 1 mm of separation between the gate electrode and the silicon dioxide. The wafer was diced using a diamond cutter and the pieces were used to scoop the graphene out of water in the process described earilier. This process is illustrated with an isometric computer rendering in Figure 9, an animated cross section in Figure 10, a microscope image in Figure 11, and images of the wafer masking process in Figure 12 and Figure 13. The resulting devices were capable of handling higher voltage without breaking down with a success rate of 100%, as seen in Figure 14. The devices are then let to anneal in vacuum. It can be seen from Figure 15 that annealing the devices in vacuum produces the same $I_d - V_g$ relation as seen in previous works [1].

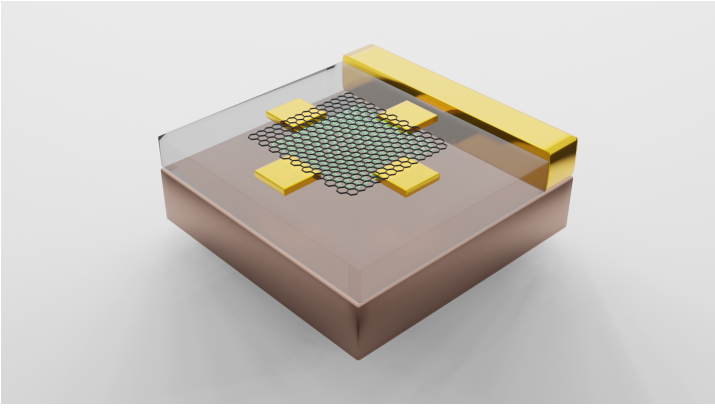

Figure 9 : Blender rendering of a graphene/SiO_2 device with a non-impregnated gate electrode.

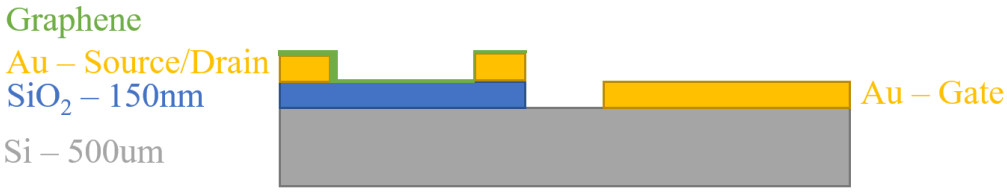

Figure 10 : Cross section of a graphene/SiO_2 device with a non-impregnated gate electrode.

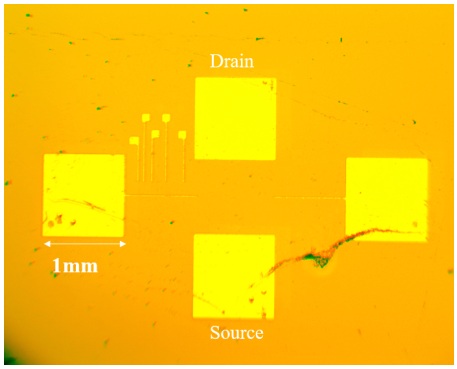

Figure 11 : Microscope image of the top view of a graphene/SiO_2 device with a non-impregnated gate electrode.

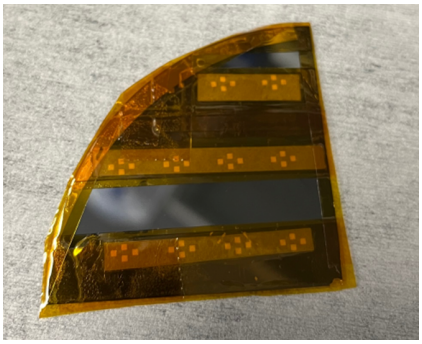

Figure 12 : Image of the masking procedure to make non-impregnated gate electrodes.

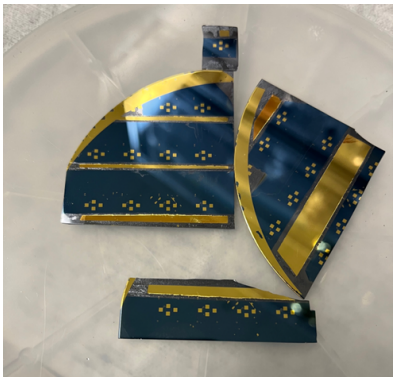

Figure 13 : Image of a finished wafer.

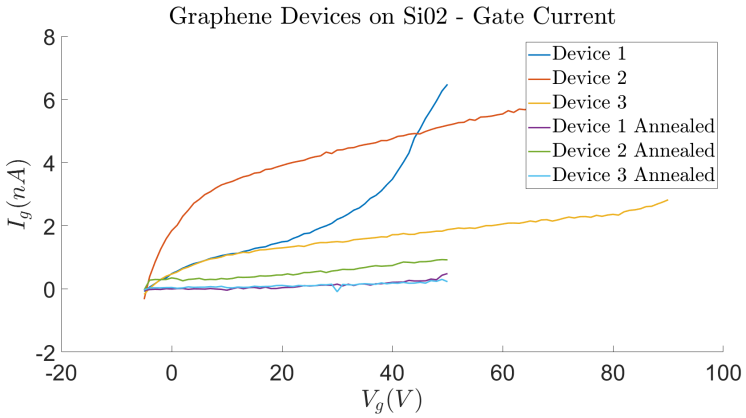

Figure 14: Gate current vs gate voltage for graphene/SiO_2 devices 1-3 before and after annealing.

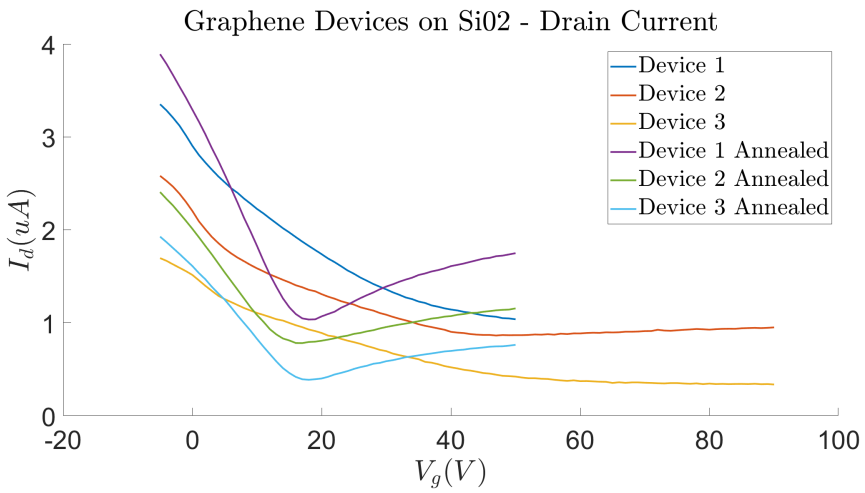

Figure 15 : Drain current vs gate voltage for graphene/SiO_2 devices 1-3 before and after annealing.

The idea of heterostructures to enhance device performance has been around for over sixty years [31]. When graphene is supported by silicon dioxide as a substrate, the carrier mobility is limited due to scattering from surface states, impurities, substrate surface roughness, and silicon dioxide surface phonons [32]. Hexagonal Boron Nitride (hBN) has a similar hexagonal lattice to graphene (1.7% lattice mismatch), is inert and insulating, and has no dangling bonds. and provide an excellent dielectric substrate for graphene [32]. Therefore, hBN substrate provides a next logical step in advancing device performance for the purposes of this thesis. The fabrication process is outlined in Figure 16 and the comparison in device quality between oxide and hBN supported devices is illustrated in Figure 17.

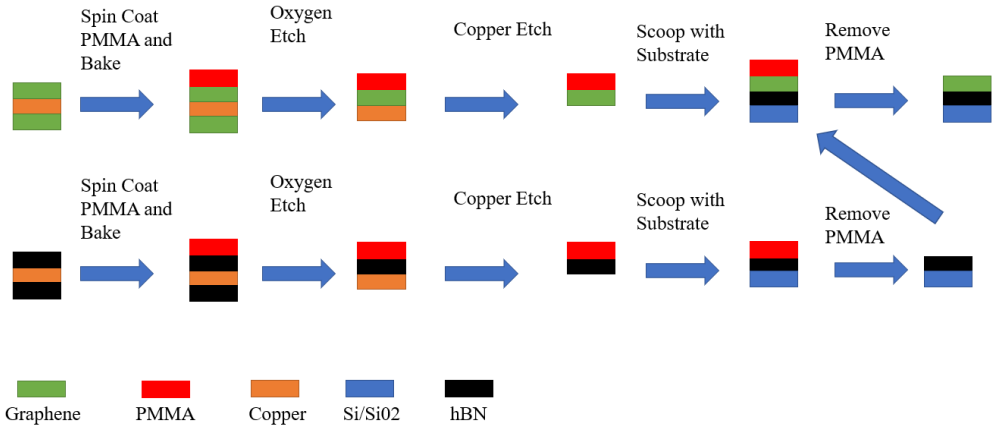

Figure 16: Fabrication process for graphene-hBN devices.

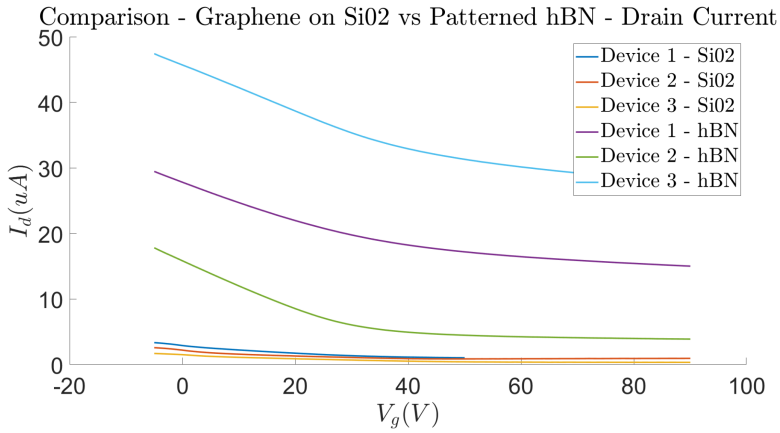

Figure 17 : Drain current vs gate voltage for graphene/SiO_2 devices 1-3 and graphene/hBN devices 1-3.

It would seem that performing the same annealing process on these devices would improve the performance as with the case of graphene on silicon dioxide. However, Figure 18 tells a different story. Devices 1 and 2 show slight improvement with annealing and Device 3 shows a slight degradation with annealing. The most noticeable feature is the fact that the Dirac point is not revealed clearly like it was in the case of the graphene on silicon dioxide. The reason for this is most likely that the photoresist used to pattern an active area of hBN is difficult to remove entirely. In Figure 19, the faint white photoresist can still be seen even after a two day

treatment in acetone. Therefore, annealing cannot remove this impurity that is clearly doping the graphene to the point where it cannot be removed. Therefore the solution to this problem is to not pattern the hBN at all, but rather to scoop it and manipulate it with rubber tweezers to a desirable location on the device. This process can be seen to significantly improve graphene's performance in Figure 20. Similar to before, annealing these samples in vacuum does not improve their performance as seen in Figure 21. It has been shown that annealing in nitrogen instead of in vacuum can improve device quality. The results from graphene devices with an unpatterned hBN substrate before and after annealing in nitrogen are shown in Figure 22. The results are comparable with [32]. This is the final stage of improvement of device quality presented in this thesis. The comparison of the devices made in this thesis with the state of the art are presented in the next section.

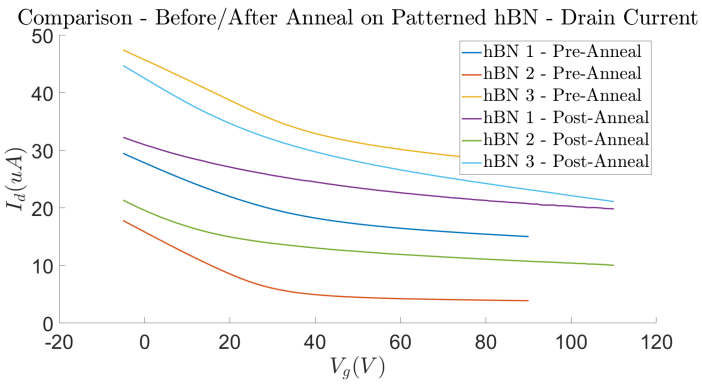

Figure 18 : Drain current vs gate voltage for graphene/hBN devices 1-3 before and after annealing. The vacuum annealing generally improves the quality, but the device does not develop the proper Dirac structure.

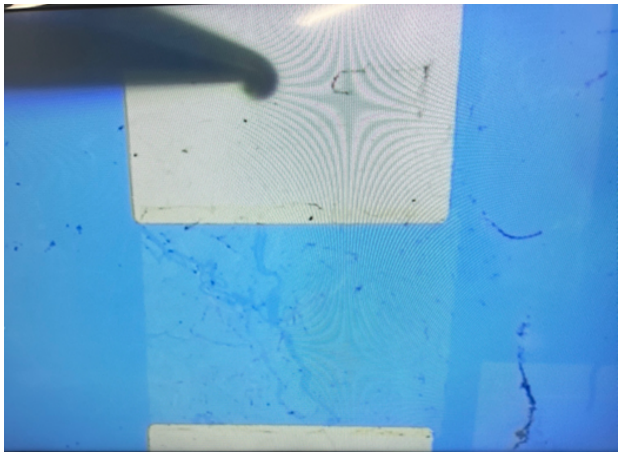

Figure 19 : Microscope image of a patterned graphene/hBN device showing the photoresist residue on the active area.

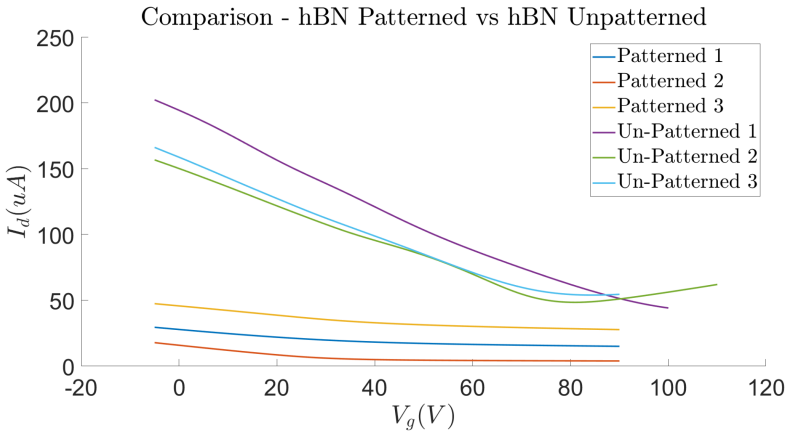

Figure 20 : Drain current vs gate voltage for patterned graphene/hBN devices 1-3 and un-patterned graphene/hBN devices 1-3. The unpatterned devices exhibit significantly higher quality.

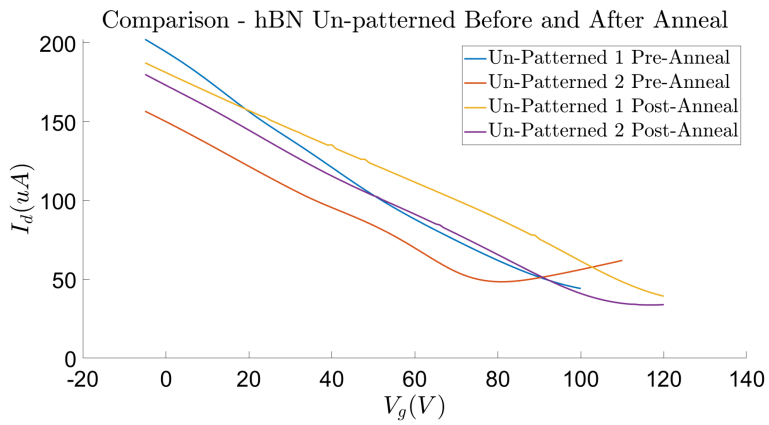

Figure 21: Drain current vs gate voltage for un-patterned graphene/hBN devices 1-2 before and after annealing in vacuum. Annealing in vacuum does not improve the quality, nor develop the Dirac point structure.

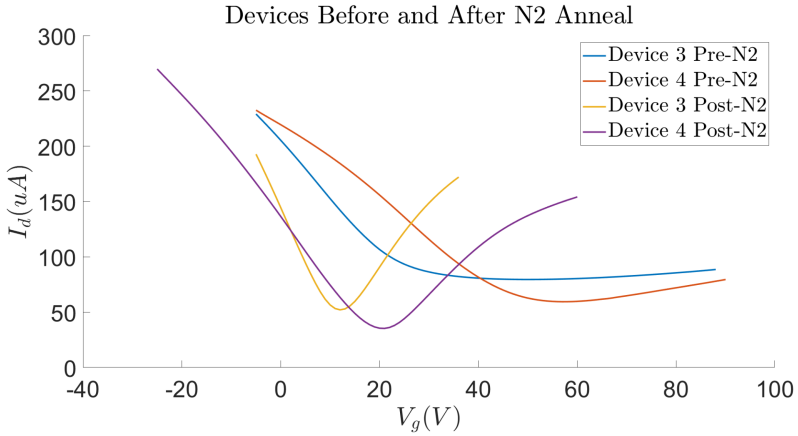

Figure 22: Drain current vs gate voltage for un-patterned graphene/hBN devices 3-4 before and after annealing in nitrogen. Annealing in nitrogen develops the Dirac structure.

Chapter 4 - DC Characterization

After the $I_d - V_g$ measurements have been taken, the carrier mobility can be extracted. Since the devices are field effect devices, the field effect mobility is first calculated. There are traditionally three methods for calculating the field effect mobility of graphene: the direct transconductance method (DTM), the transfer length method (TLM), and the fitting method (FTM) [33]. TLM requires that a transmission line structure be created to account for the contact resistance. If unaccounted for, the calculated mobility of the device will be reduced [34]. Unfortunately, for our devices, the transmission line structure could not be utilized, as it became apparent that patterning the device degraded performance. Therefore, the mobility is evaluated using DTM. For a large enough device, as is the case in this thesis (.9 mm x .9 mm), the length dependence on each of the field effect mobility calculations vanishes [34]. The commonly used "fitting" approach can also determine mobility, however that will be described in detail in a later section of this thesis [35].

The mobility of the samples were calculated using three simple methods that neglected the contact resistance, did not perform any fitting, and could calculate the mobility of the sample versus carrier concentration and gate voltage - as seen in Figure 23 and Figure 24. This was done using the formulations described by Lee [33], Bolotin [34], and Zhong [36] respectively. These methods neglect the quantum capacitance of graphene (which is usually much larger than the oxide capacitance making it negligible) [33]. Additionally, the contact resistance is neglected (it will be accounted for in a later section of the thesis), making the reported mobility significantly lower than the actual mobility [34]. It should be mentioned that the improvement of device mobility after annealing agrees with [34], as seen in Figure 25. The following equations describe

the different ways that mobility can be evaluated where μ is the mobility, σ is the conductivity, q is the fundamental charge, n_{tot} is the total carrier concentration, n is the gate voltage induced carrier concentration, g_m is the transconductance, C_{ox} is the oxide capacitance, and V_d is the drift voltage.

$$\mu_{Lee} = \frac{\sigma}{q n_{tot}} \tag{9}$$

$$\mu_{Bolotin} = \frac{\sigma}{q n} \tag{10}$$

$$\mu_{Zhong} = \frac{|g_m|}{C_{ox} V_d} \tag{11}$$

Equations 9-11 use Equations 12-17 where ϵ_0 is the free space permittivity, ϵ_r is the relative permittivity of the oxide material, d is the thickness of the oxide material, V_{Dirac} is the voltage at which the Dirac point occurs, V_g is the applied gate voltage, and I_d is the drain current.

$$C_{ox} = \frac{\epsilon_0 \epsilon_r}{d} \tag{12}$$

$$n_0 = \frac{C_{ox}}{q V_{Dirac}} \tag{13}$$

$$n = \frac{C_{ox}(V_g - V_{Dirac})}{q} \tag{14}$$

$$n_{total} = \sqrt{n_0^2 + n^2} \tag{15}$$

$$g_m = \frac{\Delta I_d}{\Delta V_g} \tag{16}$$

$$\sigma = \frac{I_d(V_g)}{V_d} \tag{17}$$

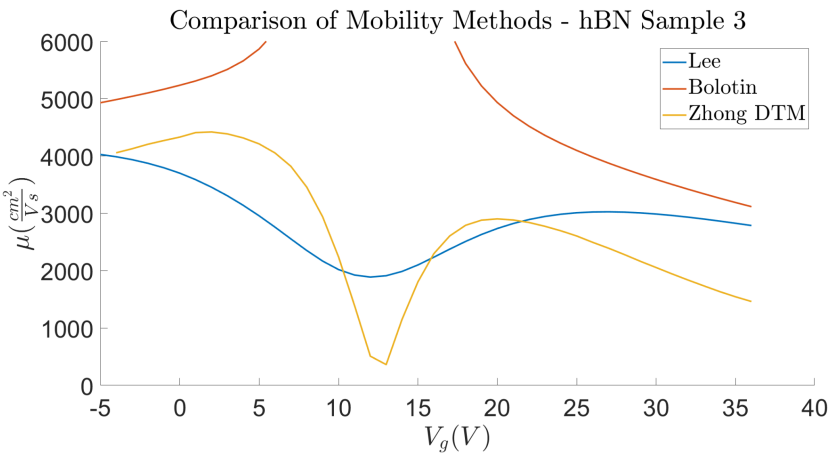

Figure 23 : Mobility evaluated using three different methods for hBN sample 3 vs the gate voltage.

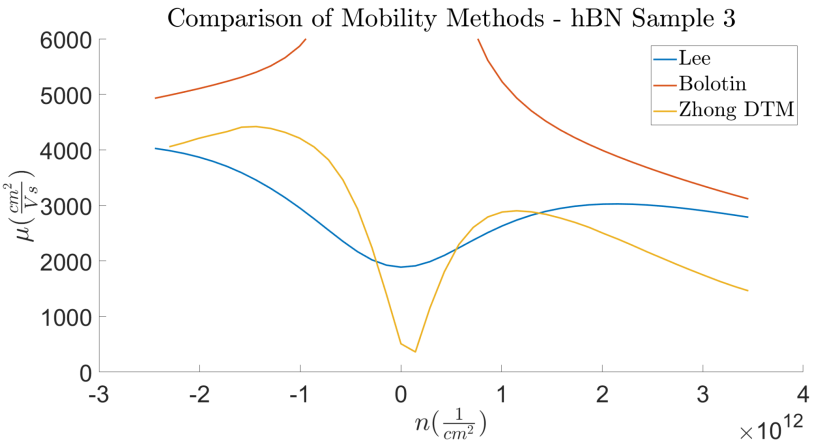

Figure 24 : Mobility evaluated using three different methods for hBN sample 3 vs the carrier concentration.

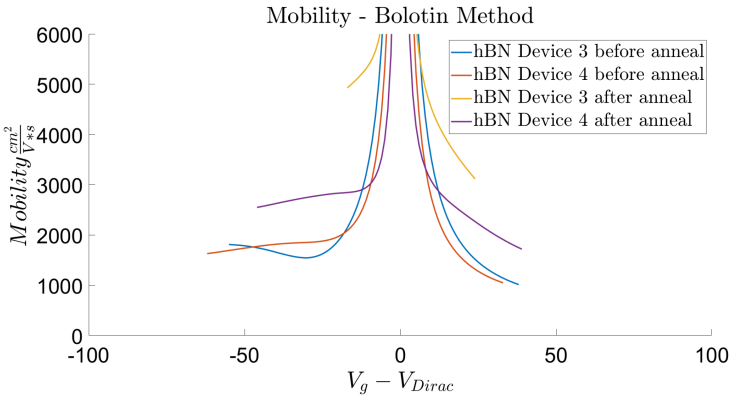

Figure 25 : Mobility vs gate voltage before and after annealing shows how annealing improves mobility.

To account for the contact resistance that was neglected in the simple methods, it is possible to fit the data using a method outlined in [35] where the contact resistance ($R_{contact}$), residual carrier concentration (n_0), and carrier independent mobility (μ) are the parameters that need to be fit to measured data. This is done with the formula outlined in [35] where R_{total} is the total resistance measured from the semiconductor analyzer and N_{sq} is the number of squares of graphene (one in this case).

$$R_{total} = R_{contact} + R_{channel} = R_{contact} + \frac{N_{sq}}{n_{total} q \mu} \tag{18}$$

Results are shown in Figure 26. The extracted mobility, contact resistance, and residual carrier concentration are $5589\ \frac{cm^2}{Vs},\ 196\ Ohms,\ and\ 6.5x10^{11}\frac{1}{cm^2}$ respectively. This is consistent with the theory that estimated mobility is reduced when contact resistance is not accounted for [34]. However the mobility extracted is carrier independent, which makes it a different model than the simple carrier dependent models used previously.

A comparison of these samples with the state of the art will be discussed here. The mobility of low temperature, suspended graphene samples can reach up to 200,000 $cm^2V^{-1}s^{-1}$ [36]. The first electrical measurement of large area (CVD graphene wet transferred onto a substrate) showed a room temperature mobility of 4000 $cm^2V^{-1}s^{-1}$ [28]. It has been shown that CVD graphene wet transferred onto hBN can reach mobilities up to 70,000 $cm^2V^{-1}s^{-1}$ at room temperature [37]. It should now be noted that while these record breaking devices are using large area graphene initially, the *active area* is always on the order of μm and not mm, like the samples discussed in this thesis. This limits their ability to be used in actual experiments that explore phenomena other than mobility measurements or to be integrated in realistic applications.

Photocurrent experiments have been performed on 30 um x 30 um CVD graphene with a mobility of up to 2000 $cm^2V^{-1}s^{-1}$ [38] .

The final metric used in this paper for evaluating graphene performance is the time to recombination. This metric can be calculated from the $I_d - V_g$ curves just like mobility. The recombination time can be calculated using the Einstein relation [39] where σ is the conductivity, n is the carrier concentration, q is the fundamental charge, and v_F is the Fermi velocity:

$$\tau = \frac{\hbar\sigma\sqrt{\pi/n}}{q^2 v_F} \tag{19}$$

Although the residual carrier concentration is relatively unimportant in determining the carrier mobility, it is important for determining the recombination time. Recombination time is not a commonly reported metric like carrier mobility; however, it is an important metric when calculating frequency-dependent conductivity required in full wave simulations to model graphene. Therefore it is important to evaluate the devices designed in this thesis with this metric, as it sets an upper limit on full wave simulation input parameters. The recombination time is an important parameter that dictates the degree of usability of graphene in future devices. For example, the Faraday rotation can be enhanced by a factor of 10 if the recombination time is increased by a factor of 10 [14]. Results for hBN sample 3 using the carrier concentration estimated by the simple formulation presented in Lee [34] as well as with the fitting technique (Equation 18) [35] are shown in Figure 27 and Figure 28. The results indicate the dependence on the calculated recombination time on the estimated carrier concentration, recalling that the residual carrier concentrations computed from the methods presented in Lee [34] and Kim [35] are $1.7x10^{12}\frac{1}{cm^2}$ and $6.5x10^{11}\frac{1}{cm^2}$, respectively.

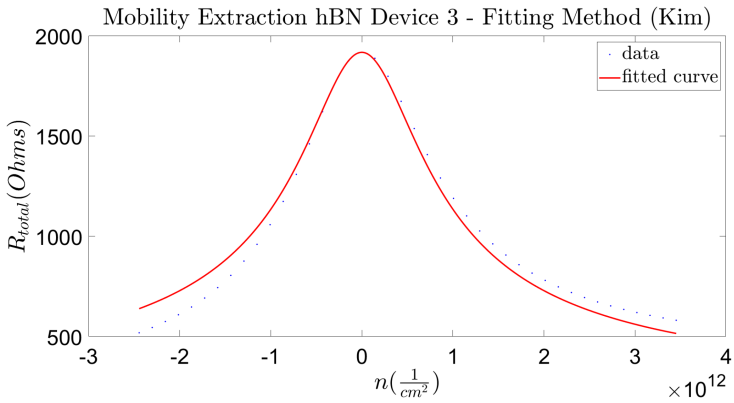

Figure 26 : Mobility extracted using the fitting method [35].

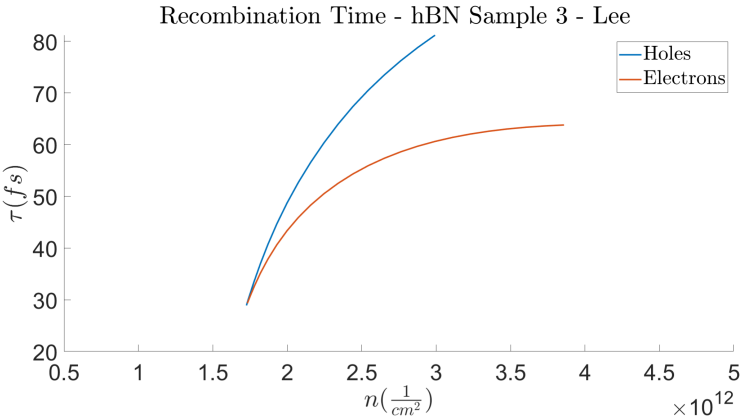

Figure 27 : Recombination time extracted from the method described by Lee [34].

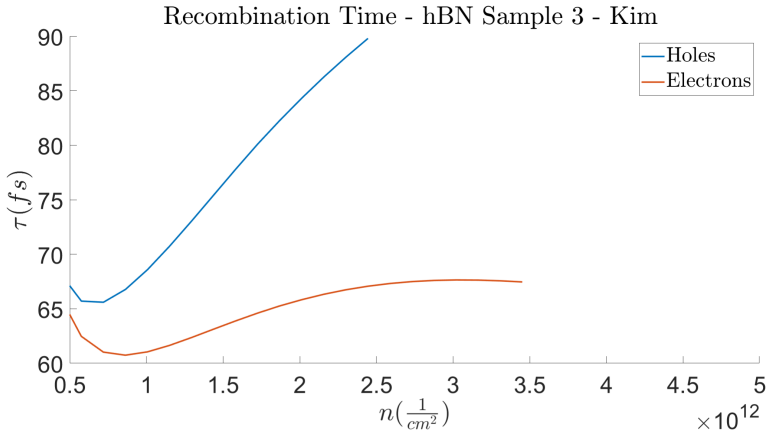

Figure 28 : Recombination time extracted from the method described by Kim [35].

Chapter 5 - IR Characterization

For detection of small photoinduced signals, lock-in detection is a common low noise solution that does not require a background measurement to subtract from the data of interest. The setup in this paper involves the use of a mechanical chopper, which modulates the laser beam in the form of a square wave by physically interrupting the beam. The fundamental frequency of this square wave is sent to the lockin amplifier as a reference signal to lock to. The measurement signal connected to the amplifier is the photocurrent coming from the source and drain electrodes connected to the graphene sample. Since the lockin amplifier is locking to the first harmonic of this signal, the actual signal can be recovered from the amplifier using the formula [40]:

$$V_{actual} = V_{LIA}\frac{\pi}{\sqrt{2}} \tag{20}$$

The experimental setup that was used in this thesis provides an external gate bias to the graphene sample using a DC power supply, a drift bias to the graphene sample using the built-in DC biasing feature of the transimpedance amplifier (which is measured in the experiment using a multimeter), polarization control using two linear polarizers (the latter of which is removed if performing studies using circular polarization) and a quarter wave plate, and automated laser power measurement using a 10-90 beam splitter as illustrated in Figure 29.

The temporal response of graphene to ultrafast photoexcitation was documented to show a millisecond response time if the gate oxide was made as thin as possible (5 nm) and high levels of light intensity are used ($> 50\ \mu W/cm^2$)[41]. The oxide thickness dependence is because the response time of graphene to ultrafast photoexcitation is largely dependent on the oxide capacitance, which is inversely related to the oxide thickness. Additionally at 5 nm thickness,

tunneling from the semiconductor to the graphene is possible, whereas this phenomenon is essentially irrelevant at larger thicknesses. The light intensity dependence is due to the charge accumulation time at the oxide/graphene interface. The temporal response documented in this thesis shows a much larger steady state response time than the one found in reference [41]. As can be seen in Figure 30, it takes ~200 seconds to reach a steady state response. The time to reach steady state drift current without a laser after toggling on the gate voltage is also ~200 seconds. It remains uncertain as to why the response takes so long to reach steady state, although the electronic instrumentation may have something to do with it. Therefore, the temporal response of *all* measurements used in this study waits 200 seconds when a parameter is varied in order to properly reflect the steady state response.

It has been shown that the Dirac point of graphene is shifted when it is under the influence of photoexcitation [42]. This is because graphene can only absorb a maximum of 2.3% of all incident photons, and transmits the rest. The transmitted photons proceed to the substrate where they generate free carriers which effectively provides an additional bias to the graphene. It makes physical sense that more photo-carriers are generated at this photo-induced Dirac point, because that is the doping level at which there are the least number of free carriers in the graphene. This phenomenon is documented in Figure 31. However, if the gate voltage is swept over a larger range away from the Dirac point, it can be seen that there is a significant photocurrent generated far away from the Dirac point. The extent of this study is limited by the range of the DC Power supply (0-120 V) as shown in Figure 32. This could be remedied by decreasing the oxide thickness in future studies.

An additional study that was done on the transient behavior was to study the temporal photoresponse at different gate biases. It can be seen that the shape of the temporal response

varies with the gate bias. Given the limited number of similar works reported in literature, the results promote a study for further investigation.

The next measurements taken on the sample are the photo-current dependence on the drift bias and laser power. It can be seen in Figure 34 that the photocurrent increases linearly as a function of the drift bias and increases asymptotically as a function of the laser power in Figure 35.

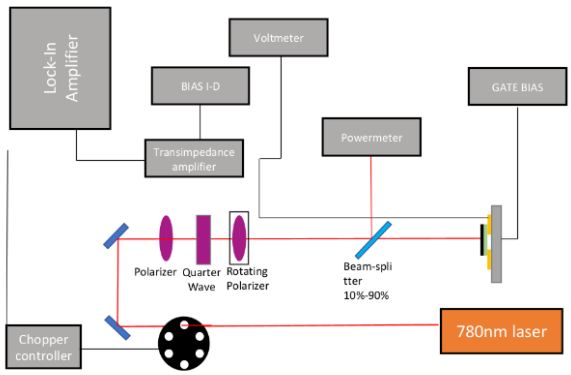

Figure 29 : Schematic of the system used to perform IR characterization of the graphene device.

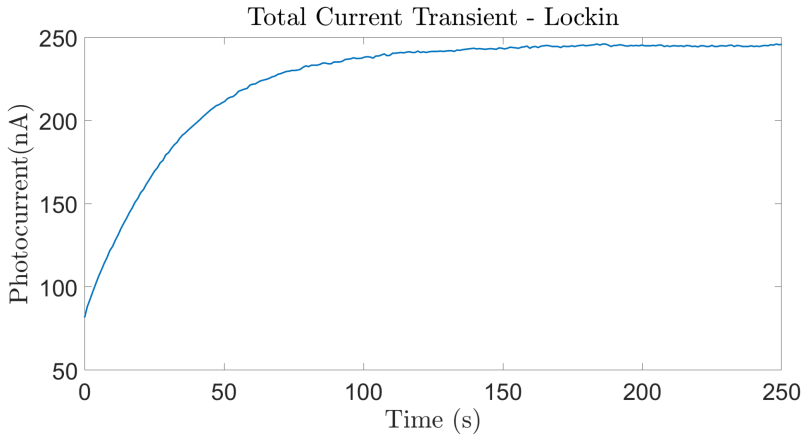

Figure 30: Measured photocurrent transient.

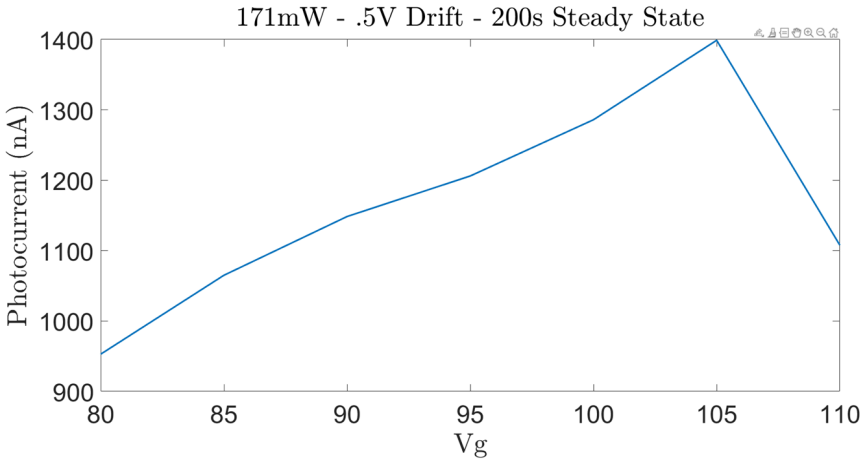

Figure 31 : Steady State photocurrent vs gate voltage around the Dirac Point

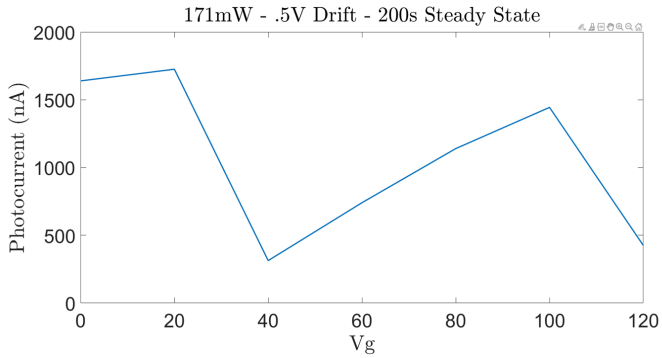

Figure 32 : Steady State photocurrent vs gate voltage for the entire range of the DC Power supply used.

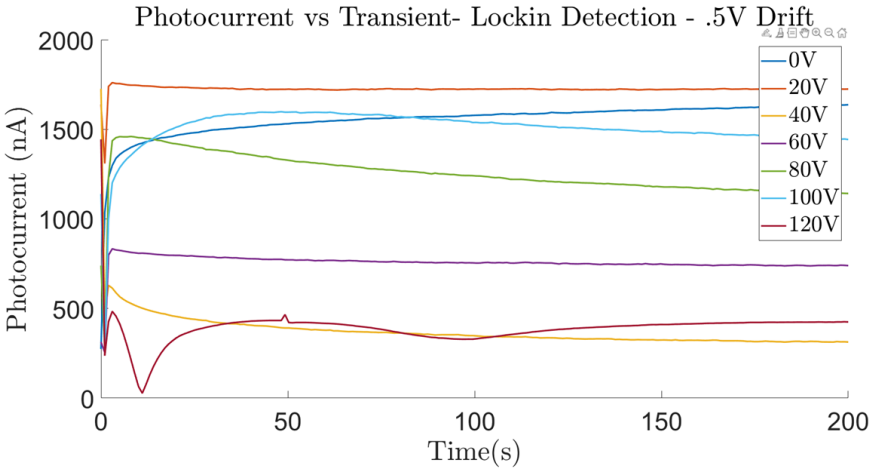

Figure 33 : Transient photocurrent for different gate voltages at 150 mW laser power.

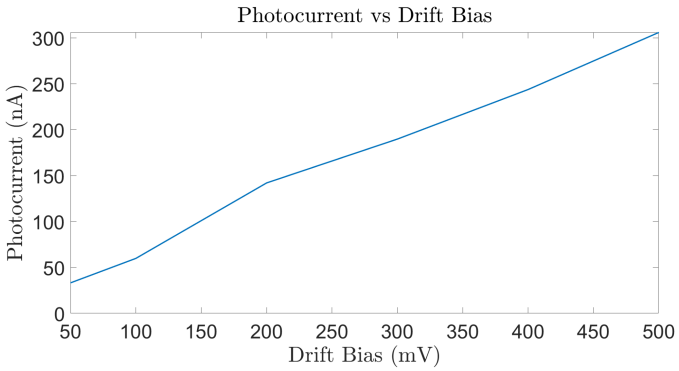

Figure 34 : Photocurrent vs drift bias. Gate bias set to 105 V and laser power set to 10 mW

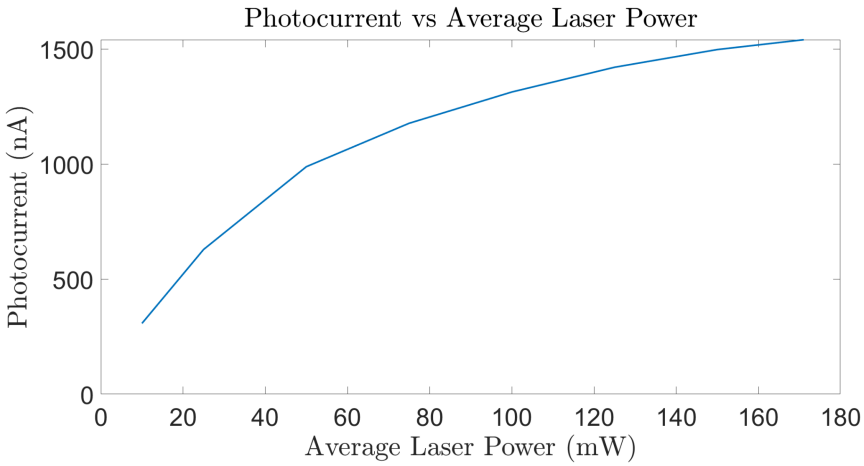

Figure 35 : Photocurrent vs Average laser power. Gate bias set to 105 V and Drift bias set to .5 V.

The polarization response of graphene to ultrafast photoexcitation has experimentally exhibited strong coupling between circular polarized light and the off-diagonal Hall conductivity [43]. Light Polarization can be controlled using waveplates. Since the input polarization of the laser is linear, a quarter wave plate is used to switch between linear polarization and two types of circular polarization, right and left-handed. A quarter wave plate has a Jones' matrix of:

$$QWP = \begin{bmatrix} 1 & 0 \\ 0 & -i \end{bmatrix} \tag{21}$$

Therefore, when an linearly polarized (*x* in this case) input is sent into the polarizer, the output can be described as a function of the angle between the quarter waveplate and the input polarization, θ,by:

$$Output = R(-\theta) * QWP * R(\theta) * \begin{bmatrix} 1 \\ 0 \end{bmatrix} \tag{22}$$

Where the rotation and anti-rotation matrices are described as:

$$R(\theta) = \begin{bmatrix} cos(\theta) & -sin(\theta) \\ sin(\theta) & cos(\theta) \end{bmatrix} \tag{23}$$

$$R(-\theta) = \begin{bmatrix} cos(\theta) & sin(\theta) \\ -sin(\theta) & cos(\theta) \end{bmatrix} \tag{24}$$

Figure 36 describes the output behavior of the waveplate as a function of the rotation angle of the waveplate. Therefore, a quarter wave plate can be a great tool to control the polarization state of light because it can be used to toggle between linear polarization and circular polarization by rotating it using a rotation stage, as was done in this thesis. Figure 37 shows that there appears to be a photocurrent dependence on the polarization state of light.

Graphene's diagonal conductivity dependence on the polarization state of light is a topic that lacks significant experimental study, and therefore should be studied further given these very interesting initial results. Given the promising results of the fabrication and photocurrent trials presented in this thesis, the future direction is to develop a sample capable of utilizing all four electrodes to compare the optically induced hall conductivity with traditional magnetically induced hall conductivity. A subsequent performance improvement process would logically follow.

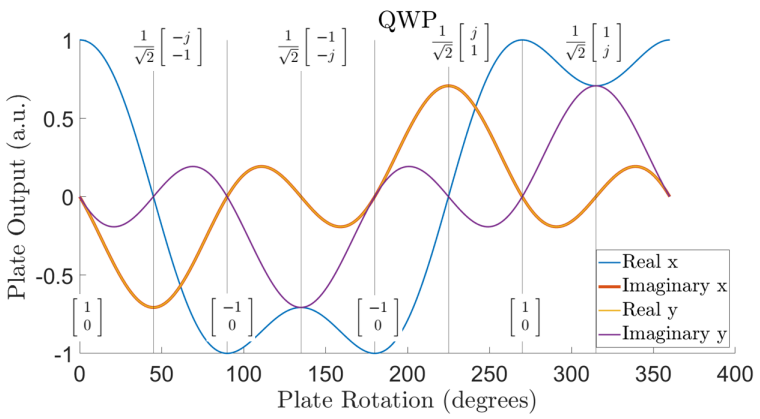

Figure 36 : Polarization state output from a QWP with a x-polarized input vs plate rotation.

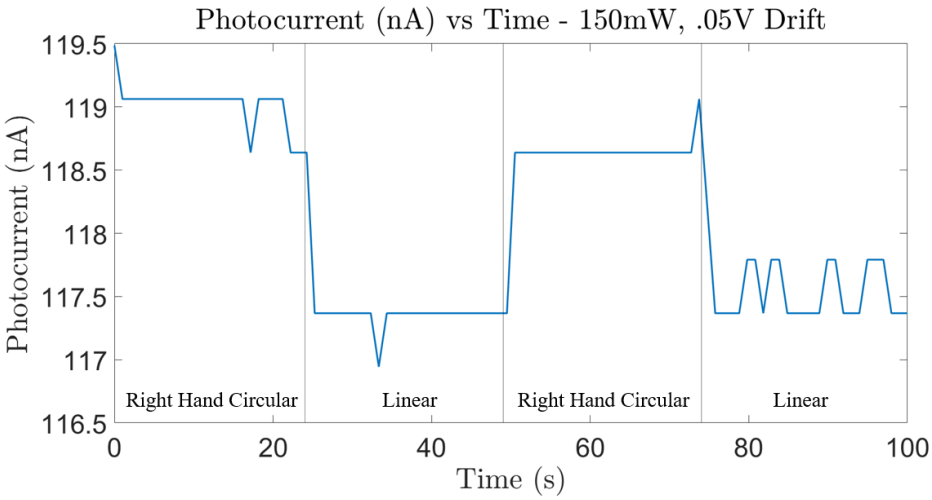

Figure 37: Steady State photocurrent vs polarization state showing an increased response with circularly polarized light.

Chapter 6 - THz Characterization

Section 6.1 - Theoretical THz Response of Graphene

The principal motivation for developing graphene devices in this thesis is to study how they interact with THz radiation. The ultimate goal of this work is to develop devices capable of demonstrating THz polarization rotation and detecting the degree of polarization rotation with the highest level of accuracy possible. Such an experiment would be highly impactful within the fields of THz science, ultrafast communication, and sensing.

The rotation of light as it passes through a medium under the influence of a magnetic field was first discovered by Micheal Faraday in 1846 [4]. This effect, known as Faraday rotation, is largely dependent on the magnitude of the magnetic field acting on a material and the length or thickness of the material. In 2003, it was discovered that an extraordinarily thin electron gas could produce significant Faraday rotation [5]. This discovery inspired the work done to discover Faraday rotation in graphene [6].

Faraday rotation has enabled the production of Faraday isolators. These devices allow light to travel in one direction while preventing light from traveling in the opposite direction. Faraday isolators are commonly paired with lasers to prevent reflections or light from other sources from reaching the laser resonator. Current Faraday isolator devices in the THz spectrum are too bulky for miniaturized applications, as ferromagnetic materials are typically employed in their construction to produce a magnetic field. In this thesis, giant Faraday rotation in ultra thin graphene under the influence of a magnetic field is simulated using COMSOL. In the simulations, up to 20 degrees of polarization rotation in single atom thick graphene is generated. This is on the order of the Faraday rotation first observed experimentally [6]. Results of these

simulations suggest that it would be possible to construct a Faraday isolator (45 degrees of polarization rotation) if a large enough magnetic field is present and high quality graphene is used.

The off diagonal conductivity is very related to Faraday rotation of graphene and is actually what produces it. The Faraday rotation angle follows the off diagonal conductivity fairly closely which makes the off diagonal conductivity interesting to study. Theoretically the Faraday angle follows Equation 25 where η_0 is the free space impedance, σ_{xy} is the off diagonal conductivity, σ_{xx} is the diagonal conductivity, and n_{sub} is the refractive index of the substrate. The equation is technically limited to frequencies below the cyclotron frequency [44], although it is shown through full wave simulations that the relation holds at frequencies above the cyclotron frequency.

$$\theta_F \approx tan^{-1}\left(\frac{\eta_0\sigma_{xy}}{1 + n_{sub} + \eta_0\sigma_{xx}}\right) \tag{25}$$

Using the Drude Model presented in Chapter 2 of this thesis, the complex conductivity of graphene with a recombination time of 183 fs, a DC conductivity of 8.011 mS, and a mobility of 5000 $cm^2V^{-1}s^{-1}$ is calculated versus frequency for an external magnetic field of 1 Tesla - which is shown in Figure 38. Subsequently, the Faraday angle for graphene of the same quality is calculated versus frequency and magnetic field as shown in Figure 39. Figure 39 shows that even at frequencies above the cyclotron frequency, the formula holds as it reproduces the same waveform from the experimental results found in [6]. This is the motivation for the experimental setup to measure the off-diagonal conductivity induced by circularly polarized optical photons. If the circular polarized light produces transverse Hall currents by utilizing the graphene's off diagonal conductivity, then the light effectively acts as a magnetic field. If the amount of Hall

current produced is measured, the conductivity can be extracted and the "effective magnetic field" produced by the laser can be quantified, and later optimized.

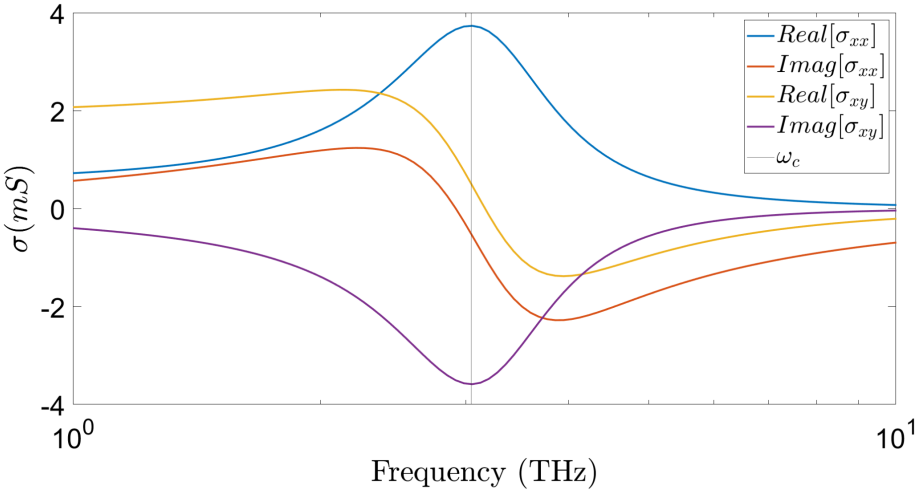

Figure 38: Complex THz conductivity tensor vs frequency for a 183 fs recombination time, 8.011 mS DC conductivity, 5000 $cm^2V^{-1}s^{-1}$ mobility sample under a 1 Tesla external magnetic field.

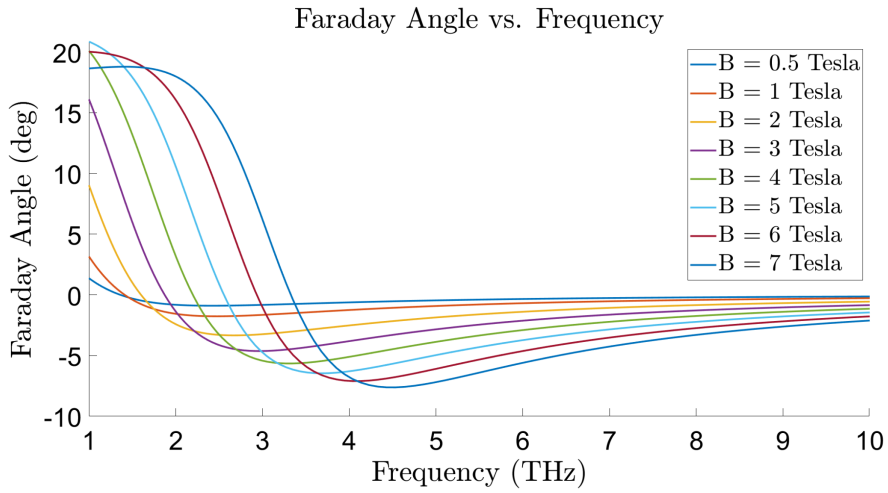

Figure 39 : Faraday rotation angle calculated using the formula presented in [44] for a 183 fs recombination time, 8.011 mS DC conductivity, 5000 $cm^2V^{-1}s^{-1}$ mobility sample under various magnetic fields.

In order to understand the Faraday effect more deeply, a graphene sheet of the same quality as described in the theoretical study was simulated in COMSOL. This was done with the Electromagnetic Waves - Frequency Domain module. An airbox with periodic boundary conditions applied to the sides and scattering boundary conditions applied to the ends had a boundary condition (the graphene sheet) defined in the middle of the box. This was done by defining the surface current density on the graphene sheet as a function of the user-defined conductivity (from the theoretical model shown previously) and the incident plane wave (background electric field). A "probe" in COMSOL was placed in the air region on the side of the graphene opposite the incident plane wave and the Faraday rotation that resulted was calculated using the formalism from [45] shown in Equations 26-27. The results shown in Figure 40 closely reproduce the results of the theoretical Faraday rotation, which motivates further study into the effect of gate biasing and quality on the Faraday angle.

$$\theta_F = 1/2 \quad tan^{-1}(\frac{\Re(2\chi)}{1-|\chi|^2}) \tag{26}$$

$$\chi = \frac{E_{y_{transmitted}}}{E_{x_{transmitted}}} \tag{27}$$

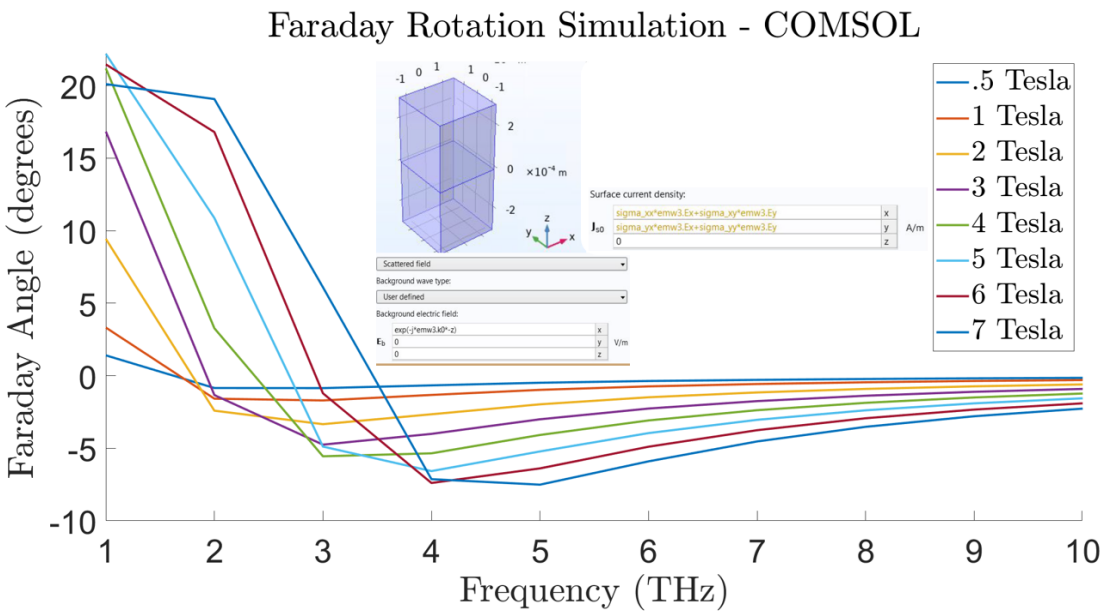

Figure 40 : Faraday rotation angle calculated from a full wave COMSOL simulation using the formula presented in [45] for a 183 fs recombination time, 8.011 mS DC conductivity, 5000 $cm^2V^{-1}s^{-1}$ mobility sample under various magnetic fields.

Section 6.2 - Experimental THz Response of Graphene

The THz system used to characterize the graphene samples in this thesis was the Menlo Systems Tera-K15. The system was driven by a femtosecond (80 fs) Erbium-fiber laser (1560 nm) which illuminated a photoconductive antenna that radiated in THz region (.1-3.5 THz). After careful alignment of the emitter and detector and the four lenses between them, a sample can be placed in the center of the system. When a silicon sample is placed in the THz beam path, there is both attenuation and delay of the signal. Additionally, there is a Fabry-Perot resonance which is the small delay pulse. This effect is a result of the reflections within the silicon sample. Another observation that can be made is that the silicon sample with the hBN/graphene stack has a noticeably smaller signal. The reason for this is that graphene is conductive at THz. What is

remarkable is that its effect is noticeable even though it is only one atom thick. The results of the measurement are shown in Figure 41.

The refractive index of the substrate must be calculated numerically after taking THz TDS measurements with and without a substrate in the beam path. This is done by solving for the thickness of the substrate as well as the real and imaginary parts of the refractive index numerically through the Transfer Matrix Method [46]. The measured transfer function can be written in Equation 28 with $E_{substrate}$ and E_{air} as the electric field spectrum recorded at the THz receiver when a substrate is and isn't in the beam path:

$$T_{meas} = \frac{E(\omega)_{substrate}}{E(\omega)_{air}} \tag{28}$$

The modeled transfer function can be calculated through the Transfer Matrix Method. Assuming a single layer of substrate (in this case, silicon), which has a refractive index:

$$n_{sub} = n - jk \tag{29}$$

then the method can be summarized as follows. First, a matching matrix defined by the Fresnel coefficients relates the incident wave to the wave that is transmitted to the substrate:

$$\begin{bmatrix} E_{1+} \\ E_{1-} \end{bmatrix} = \frac{1}{\tau_1} \begin{bmatrix} 1 & \rho_1 \\ \rho_1 & 1 \end{bmatrix} \begin{bmatrix} E_{1+'} \\ E_{1-'} \end{bmatrix} \tag{30}$$

Next, a propagation matrix allows the wave with wave number, k, to move through the substrate of thickness, l:

$$\begin{bmatrix} E_{1+} \\ E_{1-} \end{bmatrix} = \frac{1}{\tau_1} \begin{bmatrix} 1 & \rho_1 \\ \rho_1 & 1 \end{bmatrix} \begin{bmatrix} e^{jk_1 l_1} & 0 \\ 0 & e^{-jk_1 l_1} \end{bmatrix} \begin{bmatrix} E_{2+} \\ E_{2-} \end{bmatrix} \tag{31}$$

Finally, another matching matrix that allows the wave to exit the substrate:

$$\begin{bmatrix} E_{1+} \\ E_{1-} \end{bmatrix} = \frac{1}{\tau_1} \begin{bmatrix} 1 & \rho_1 \\ \rho_1 & 1 \end{bmatrix} \begin{bmatrix} e^{jk_1 l_1} & 0 \\ 0 & e^{-jk_1 l_1} \end{bmatrix} \begin{bmatrix} 1 & \rho_2 \\ \rho_2 & 1 \end{bmatrix} \begin{bmatrix} E_{2+'} \\ 0 \end{bmatrix} \quad (32)$$

Where the Fresnel coefficients are defined using the refractive indices for air, n_{air}, and the substrate, n_{sub} ,(for normal incidence):

$$\rho_1 = \frac{n_{air} - n_{sub}}{n_{air} + n_{sub}} \quad (33)$$

$$\rho_2 = \frac{n_{sub} - n_{air}}{n_{sub} + n_{air}} \quad (34)$$

$$\tau_1 = \frac{2n_{air}}{n_{air} + n_{sub}} \quad (35)$$

The modeled transfer function can then be found as follows:

$$\begin{bmatrix} E_{1+} \\ E_{1-} \end{bmatrix} = \begin{bmatrix} A & B \\ C & D \end{bmatrix} \begin{bmatrix} E_{2+'} \\ 0 \end{bmatrix} \quad (36)$$

$$E_{1+} = (A)E_{2+'} \quad (37)$$

$$T_{model} = \frac{E_{2+'}}{E_{1+'}} = \frac{1}{A} \quad (38)$$

The modeled transfer function is calculated and compared with the measured transfer function via an error function. The difference in magnitude and phase for each frequency measured by the THz detector is calculated as [47]:

$$mER = |T_{meas}| - |T_{model}| \quad (39)$$

$$pER = < T_{meas} - < T_{model} \quad (40)$$

The error for each frequency is then:

$$ER(\omega) = mER + pER \quad (41)$$

The total error for the refractive index tested is:

$$ER_{total} = \Sigma ER(\omega) \tag{42}$$

The refractive index is then modified via gradient descent as follows:

$$n_{i+1} = n_i - \epsilon * pER_i \tag{43}$$

$$k_{i+1} = k_i - \epsilon * mER_i \tag{44}$$

where ε is a parameter that controls the amount of change applied to each variation. In this work, ε is set to .0001. A good first guess of the refractive index of the silicon is:

$$n_{sub_1} = \frac{t_{delay}c}{thickness} + n_{air} \tag{45}$$

Where the time delay(t_{delay}) between the reference (air) pulse and the measurement pulse (silicon), the speed of light (c), the thickness of the sample, and the refractive index of air (n_{air}) make up the equation. This process is iterated 100 times until values for the real and imaginary parts of the refractive index are found, such that the total error figure of merit is minimized. Then, a new value for the thickness is tested and the process starts over again. The results for a silicon chip cut from 500 $\mu m \pm 25\ \mu m$ thick wafers are shown in Figure 42. They show that the thickness of the sample is ~490 μm.

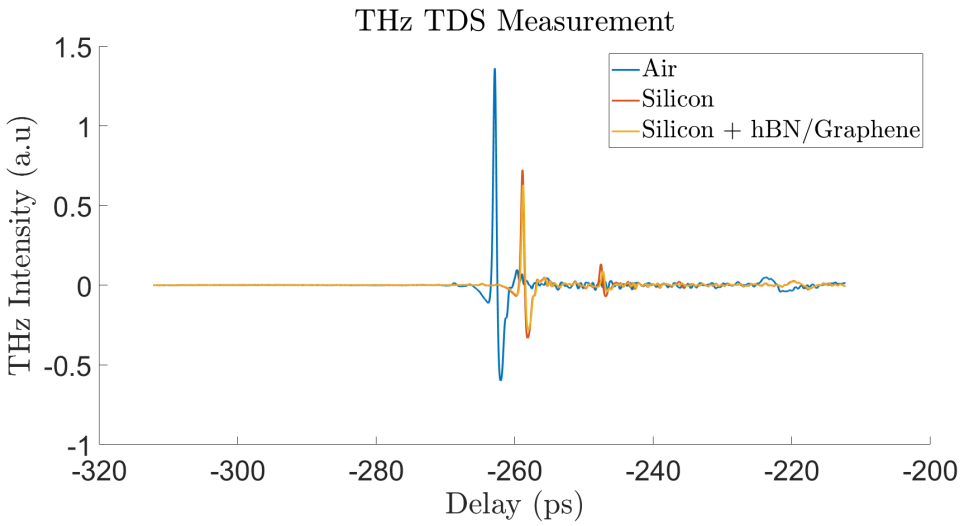

Figure 41 : THz-TDS time domain pulse data for various samples.

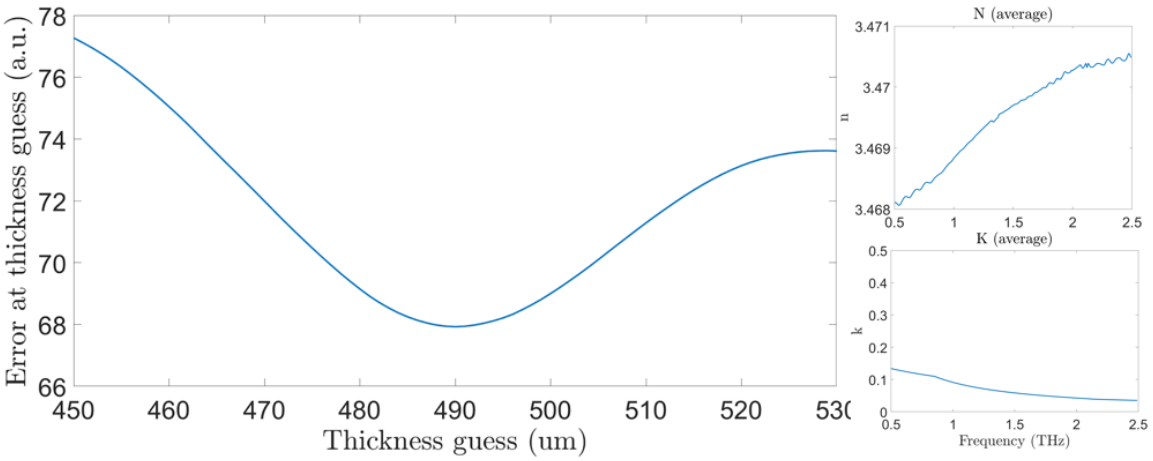

Figure 42 : Error vs thickness plot demonstrating how the thickness and the complex permittivity of the sample can be determined using the minimum error technique [47].

After the refractive index and thickness of the substrate have been measured, the THz conductivity of graphene can be calculated with the formulation using Z_0 as the free space impedance and T_G and T_{sub} as the electric field spectrum recorded at the THz receiver when there is the substrate with and without graphene in the beam path, respectively. [48]:

$$S(w) = \frac{|T_G|}{|T_{sub}|} \tag{46}$$

$$\sigma = \frac{n_{sub}+1}{Z_0}\left(\frac{1}{S(\omega)} - 1\right) \tag{47}$$

$$\Delta\sigma = -\frac{\Delta T}{T}\frac{n_{sub}+1}{Z_0} \tag{48}$$

Figure 43 compares the THz conductivity of two identical graphene samples on SiO_2/Si substrates, except one of the samples has a layer of hBN underneath. Figure 43 reveals two important features. First, the conductivity is increased when hBN is used as the immediate substrate to graphene. Second, the graphene behaves inductive at THz in both cases with the imaginary part of the conductivity less than zero, which can be seen mathematically with Equations 49-50, where *L* is the inductance and *R* is the resistance:

$$Z = R + j\omega L \tag{49}$$

$$G = \frac{1}{Z} = \frac{1}{R + j\omega L} \tag{50}$$

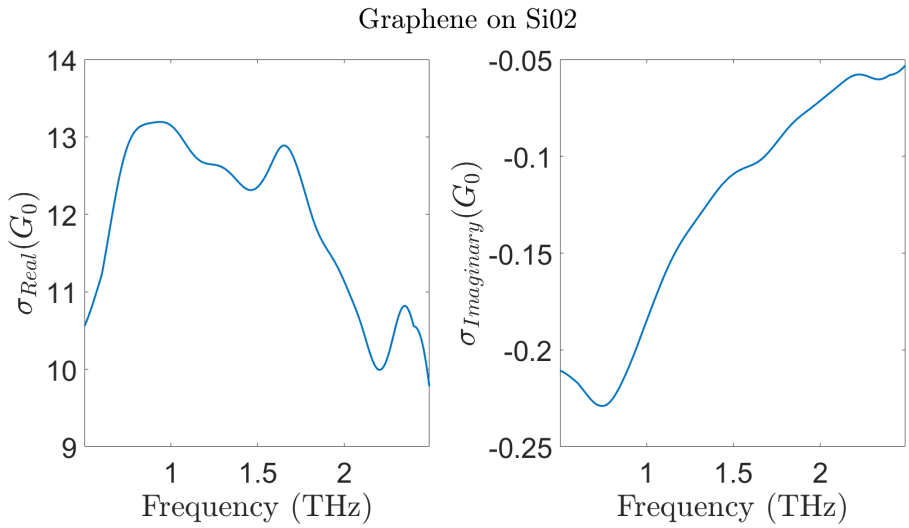

Figure 43 : Graphene conductivity in terms of $G_0 = \frac{q^2}{4\hbar}$ calculated from the formula demonstrated in [48] for graphene supported by SiO_2.

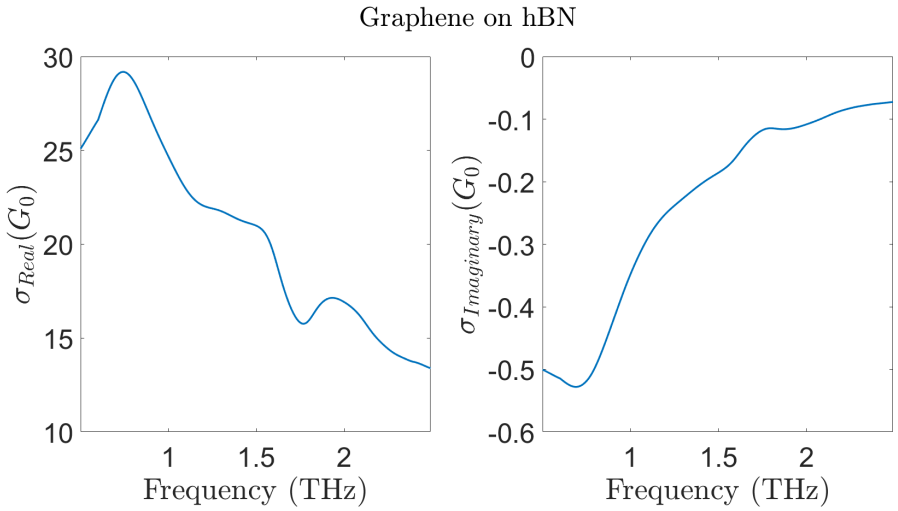

Figure 44 : Graphene conductivity in terms of $G_0 = \frac{q^2}{4\hbar}$ calculated from the formula demonstrated in [48] for graphene supported by hBN.

Another degree of freedom that the system is capable of is tuning the gate bias. This changes the chemical potential and the Fermi level and can enable reaching the Dirac Point where excess carriers are minimized and graphene is made to be as intrinsic as possible. This effect can be seen at DC with standard $I_d - V_g$ curves generated from a semiconductor analyzer system. It can also be seen at THz using THz Time Domain Spectroscopy (TDS) techniques, as seen in Figure 45. Additionally, the THz conductivity of both cases can be analyzed. It can be seen from Figure 46 that when the graphene gets closer to the Dirac point, its conductivity decreases. This is in line with the Drude formulation and the $I_d - V_g$ measurements seen earlier.

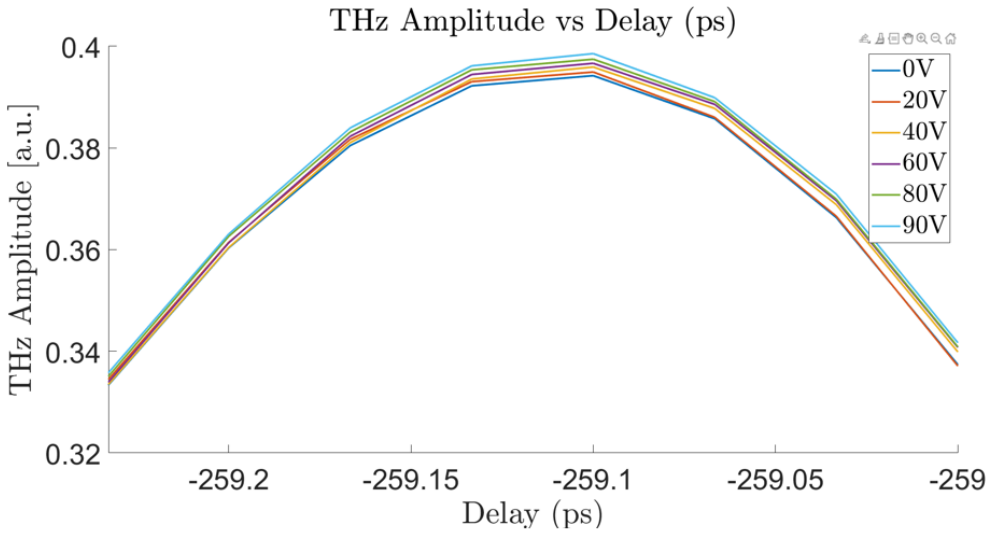

Figure 45: THz response to gated graphene for various gate voltages.

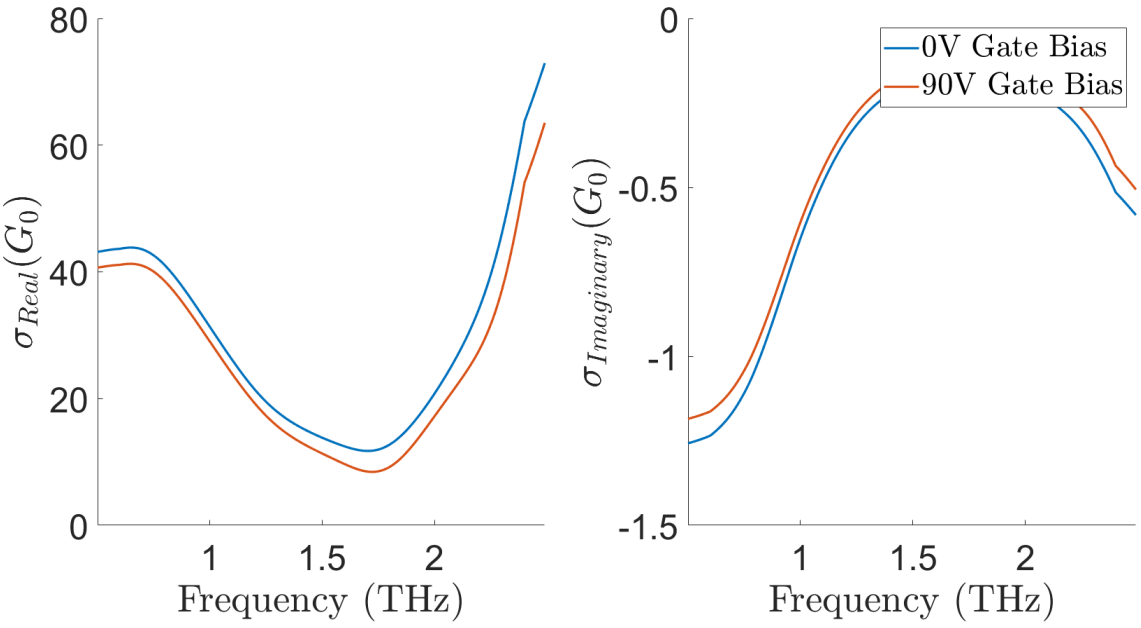

Figure 46 : THz conductivity in terms of $G_0 = \frac{q^2}{4\hbar}$ for gate biases near (90 V) and away from (0 V) the Dirac point.

Section 6.3 - THz Beam Characterization and Faraday Rotation Setup

The size of any Gaussian beam, such as that produced by the THz photoconductive antenna (PCA) and by the infrared laser can be characterized by a simple knife edge experiment. The size of the laser beam is important because the laser intensity is directly related to the laser induced electric field generated on the graphene. The size of the THz beam is important because it dictates minimum sample size, as the sample size should be greater than or equal to the size of the THz beam.

The characterization requires that a knife edge is moved through the beam path using a micromanipulator. In the results presented in this thesis, the micromanipulator is a GPIB controlled actuator mounted to a precision stage. The result of moving the knife through the beam in front of the detector is the complementary error function. When differentiated, this produces a Gaussian, as shown in Figure 47.

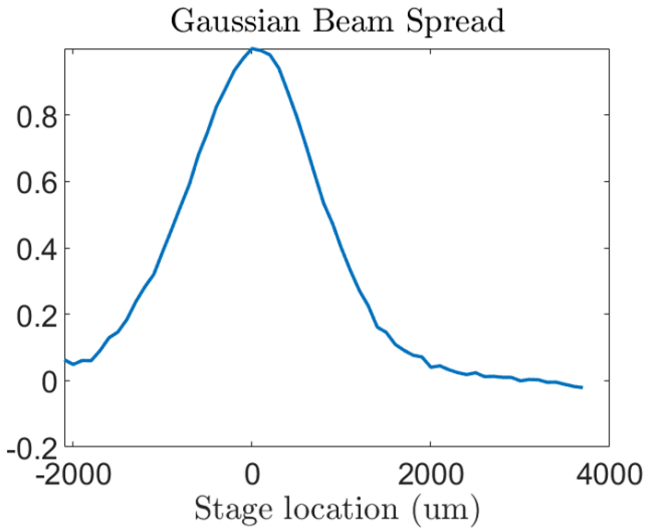

Figure 47: Results from a knife edge experiment performed on a THz beam.

Determining the THz Faraday rotation induced by photoexcited graphene can be done experimentally by accounting for Malus' Law. This physical law states that if linearly polarized light is sent through a linear polarizer and the polarizer is rotated, the output power from the polarizer will follow a $cos^2(x)$ relationship . This effect is demonstrated in Figure 48, where a linear polarizer is placed in the path of the THz beam and is rotated using a GPIB controlled rotation stage.

As can be seen from Figure 48, the sensitivity to the change in THz intensity occurs when the polarizer is rotated to 45 degrees. This observation allows for a sensitive measurement of the Faraday rotation induced by a sample with only two measurements, one measurement by rotating the analyzer to -45 degrees and the other by rotating the analyzer to +45 degrees. There will inevitably be a mismatch between the input polarizer and the analyzer, θ, when trying to identify the Faraday angle, *F*, that will actually not impact the final results due to the following formulation:

$$I = I_0 cos^2(\theta) \tag{51}$$

$$\frac{I_{-45}}{I_{+45}} = \frac{I_0 cos^2(\theta - 45)}{I_0 cos^2(\theta + 45)} \tag{52}$$

$$\frac{I_{+45}}{I_{-45}} = \frac{I_0 cos^2(\theta + F) cos^2(F - 45)}{I_0 cos^2(\theta + F) cos^2(F + 45)} \tag{53}$$

$$\frac{I_{+45}}{I_{-45}} = \frac{cos^2(F - 45)}{cos^2(F + 45)} \tag{54}$$

The frequency dependent Faraday rotation and detection can be simulated by placing a polarizer between the input polarizer and the analyzer and setting it to the "effective Faraday angle", F. In

doing this, the frequency dependent error of the "Faraday polarizer", F_0, needs to be accounted for:

$$\frac{I_{+45}}{I_{-45}} = \frac{cos^2(F + F_0 - 45)}{cos^2(F + F_0 + 45)} \tag{55}$$

and subsequently the "Faraday angle" can be found by solving the following equation numerically:

$$0 = \frac{cos^2(F + F_0 - 45)}{cos^2(F + F_0 + 45)} - \frac{I_{+45}}{I_{-45}} \tag{56}$$

When the "Faraday polarizer" is placed in the beam path and tilted to 4 degrees, the previously mentioned formulation can be implemented to calculate the frequency dependent "Faraday rotation" in a nitrogen purged environment to provide the results displayed in Figure 49.

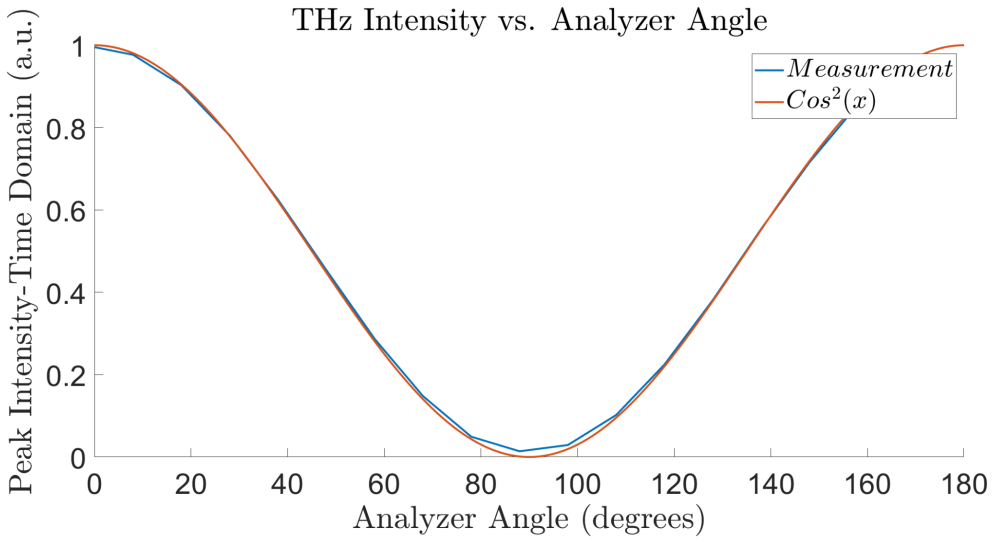

Figure 48 : Results from a THz Intensity vs linear polarizer rotation angle.

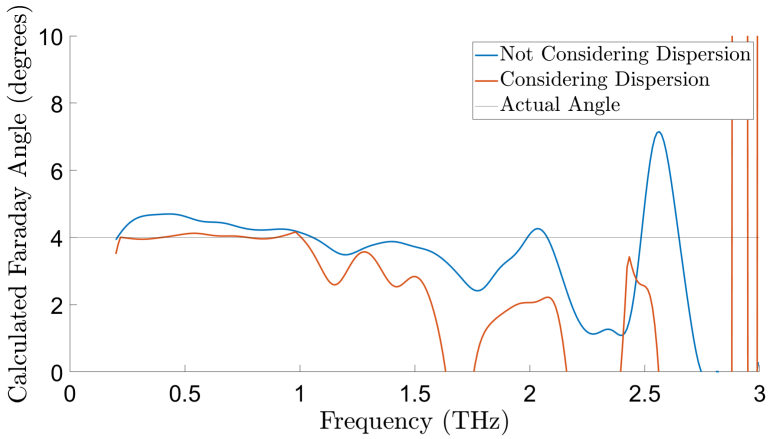

Figure 49 : Results from THz Faraday angle experiment showing with and without the necessary dispersion correction.

The results indicate that it is possible to determine the Faraday angle produced by a sample within 1/10 degree accuracy between .2 THz-1 THz. The bandwidth of the measurement can be increased by increasing the level of atmospheric purge in the system or bettering the calibration of the THz detector and emitter.

The results of the THz experiments demonstrate a methodology to determine the THz conductivity of graphene devices and show how it can be modulated using a gate bias. The results also show that it is possible to determine the Faraday rotation of a graphene sample within 1/10 degree, the precision of the mechanical rotators. This allows for future work to characterize THz Faraday rotation using graphene stimulated by non-magnetic methods. These include ultrafast optical stimulation, strain engineering, and nano-patterning

Chapter 7: Conclusion

Improvements to THz technology will enable a vast area of research, essentially creating a new science. Applications of THz include sensing, communications, biological applications, and astronomical applications [49]. THz technology will make a serious impact in the field of biomedical imaging, as THz imaging of biological tissue is capable of observing intermolecular vibrations, as opposed to intramolecular vibrations commonly observed with infrared imaging [50]. This new observation mode gives much more information on the dynamic behavior of large molecules, such as those found within the human body. THz is also capable of identifying changes in molecules (polymorphs) due to heating [51]. This has potential applications for studying the effects of long term exposure of human tissue to microwaves or other commonly encountered electromagnetic waves. A final biomedical application is using THz waves to detect skin cancer or cancers that express biomarkers through sweat or saliva [52]. Due to high THz absorption in polar molecules such as water, areas that exhibit different hydration levels in tissue (such as cancer cells) can be more easily detected with THz than with other imaging modalities. Recently, it has been observed that the magnetic field generated from THz can in fact induce a Faraday rotation of optical light in organic materials [53]. All of these biomedical applications are exciting, however improvements in the devices that interact with the THz spectrum will enable entirely new capabilities.

Such capabilities have been explored in this thesis - such as Faraday rotation and THz sensing. However, to understand how to optimize the response in the THz spectrum, it is necessary to understand how to optimize the response of graphene at DC and with optical frequencies. This optimization process and ensuing experimerimentation was carried out systematically and methodically throughout the works described in this thesis. The DC response

of various graphene devices was studied, and the quality was improved by over two orders of magnitude by implementing state of the art fabrication techniques. The ultrafast IR response of graphene was studied with a 780 nm, 80 fs laser with state of the art measurement techniques. The IR response was characterized in the transient, as well as the steady state, by varying both the gate and drift voltage, the laser power, and the input polarization state of light. Interesting results from these experiments will provide avenues for further exploration. Finally, the response of graphene to THz has been characterized as a function of frequency and gate voltage. A methodology for measuring the THz Faraday rotation has been designed and implemented.

With all of the exciting progress and results presented in this thesis, future work in the field will be interesting. For one example, it has been shown that using THz-TDS, one can simultaneously measure the Faraday and Kerr rotations in [13]. For another example, it has been shown that photoexcited graphene exhibits negative photoconductivity at THz [54], [55]. Since our devices have a gate electrode, they are capable of biasing the graphene to the Dirac point, demonstrating this phenomenon [56]. Additionally, it has recently been shown that graphene demonstrates interesting phenomena with both IR and THz [57]. Finally, the most exciting proposal has been that introducing strain to a sheet of graphene will induce a pseudo magnetic gauge field. However if this device can experimentally demonstrate giant Faraday rotation at THz frequencies using only an ultrafast optical pulse to induce the rotation, it will be the fastest THz polarization modulator yet produced, as well as the only one not requiring an external magnetic field. This one demonstration has the potential to revolutionize the entire field of THz science and bring it to mainstream society.

References

[1] Novoselov, K. S., et al. “Electric Field Effect in Atomically Thin Carbon Films.” *Science*, vol. 306, no. 5696, 2004, pp. 666–669., https://doi.org/10.1126/science.1102896.

[2] Geim, A. K. & Novoselov, K. S. The rise of graphene. *Nature Mater.* 6, 183–191 (2007).

[3] Peiponen, K. -E, et al. *Terahertz Spectroscopy and Imaging*. Springer, 2013.

[4] Faraday, M. On the magnetization of light and the illumination of magnetic lines of force. *Phil. Trans. R. Soc.* 136, 104–123 (1846).

[5] Suzuki, M., Fujii, K., Ohyama, T., Kobori, H. & Kotera, N. Far-infrared resonant Faraday effect in semiconductors. *J. Phys. Soc. Jpn* 72, 3276–3285 (2003).

[6] Crassee, Iris, et al. “Giant Faraday Rotation in Single- and Multilayer Graphene.” *Nature Physics*, vol. 7, no. 1, 2010, pp. 48–51., https://doi.org/10.1038/nphys1816.

[7] Shimano, R., Yumoto, G., Yoo, J. *et al.* Quantum Faraday and Kerr rotations in graphene. *Nat Commun* 4, 1841 (2013). https://doi.org/10.1038/ncomms2866

[8] Han, Xingyue, et al. “Giant Intrinsic Anomalous Terahertz Faraday Rotation in the Magnetic Weyl Semimetal Co2MnGa at room temperature .” *Physical Review B*, vol. 105, no. 17, 2022, https://doi.org/10.1103/physrevb.105.174406.

[9] Li, Teng-Fei, et al. “Terahertz Faraday Rotation of Magneto-Optical Films Enhanced by Helical Metasurface.” *Applied Physics Letters*, vol. 116, no. 25, 2020, p. 251102., https://doi.org/10.1063/5.0009704.

[10] Yuan, S., Chen, L., Wang, Z. *et al.* On-chip terahertz isolator with ultrahigh isolation ratios. *Nat Commun* 12, 5570 (2021). https://doi.org/10.1038/s41467-021-25881-0

[11] A. Shuvaev, G. Astakhov, A. Pimenov, C. Brüne, H. Buhmann, and L. Molenkamp, "Giant magneto-optical Faraday effect in HgTe thin films in the terahertz spectral range," Phys. Rev. Lett. 106, 107404 (2011). https://doi.org/10.1103/PhysRevLett.106.107404

[12] Arikawa, Takashi, et al. "Giant Tunable Faraday Effect in a Semiconductor Magneto-Plasma for Broadband Terahertz Polarization Optics." *Optics Express*, vol. 20, no. 17, 2012, p. 19484., https://doi.org/10.1364/oe.20.019484.

[13] Okada, Ken N., et al. "Terahertz Spectroscopy on Faraday and Kerr Rotations in a Quantum Anomalous Hall State." *Nature Communications*, vol. 7, no. 1, 2016, https://doi.org/10.1038/ncomms12245.

[14] Slipchenko, Tetiana M., et al. "Strain-Induced Large Faraday Rotation in Graphene at Subtesla External Magnetic Fields." *Physical Review Research*, vol. 1, no. 3, 2019, https://doi.org/10.1103/physrevresearch.1.033049.

[15] Tokman, I. D., et al. "Inverse Faraday Effect in Graphene and Weyl Semimetals." *Physical Review B*, vol. 101, no. 17, 2020, https://doi.org/10.1103/physrevb.101.174429.

[16] Castro Neto, A. H., Guinea, F., Peres, N. M. R., Novoselov, K. S. & Geim, A. K. The electronic properties of graphene. *Rev. Mod. Phys.* 81, 109–162 (2009).

[17] Du, Xu, et al. "Approaching Ballistic Transport in Suspended Graphene." *Nature Nanotechnology*, vol. 3, no. 8, 2008, pp. 491–495., https://doi.org/10.1038/nnano.2008.199.

[18] Calado, V. E., et al. "Ballistic Transport in Graphene Grown by Chemical Vapor Deposition." *Applied Physics Letters*, vol. 104, no. 2, 2014, p. 023103., https://doi.org/10.1063/1.4861627.

[19] Banszerus, Luca, et al. “Ballistic Transport Exceeding 28 um in CVD Grown Graphene.” *Nano Letters*, vol. 16, no. 2, 2016, pp. 1387–1391., https://doi.org/10.1021/acs.nanolett.5b04840.

[20] Nair, R. R., et al. “Fine Structure Constant Defines Visual Transparency of Graphene.” *Science*, vol. 320, no. 5881, 2008, pp. 1308–1308., https://doi.org/10.1126/science.1156965.

[21] Liu, M., Yin, X., Ulin-Avila, E. *et al.* A graphene-based broadband optical modulator. *Nature* 474, 64–67 (2011). https://doi.org/10.1038/nature10067

[22] Wang, Feng, et al. “Gate-Variable Optical Transitions in Graphene.” *Science*, vol. 320, no. 5873, 2008, pp. 206–209., https://doi.org/10.1126/science.1152793.

[23] Kuzmenko, A. B., van Heumen, E., Carbone, F. & van der Marel, D. Universal optical conductance of graphite. *Phys. Rev. Lett.* 100, 117401 (2008).

[24] Gusynin, V. P. & Sharapov, S. G. Unconventional integer quantum Hall effect in graphene. *Phys. Rev. Lett.* 95, 146801 (2005).

[25] V. P. Gusynin and S. G. Sharapov, “Transport of Dirac quasiparticles in graphene: Hall and optical conductivities,” Phys. Rev. B, vol. 73, p. 245411, 2006

[26] V. P. Gusynin, S. G. Sharapov, and J. P. Carbotte, “On the universal ac optical background in graphene,” New J. Phys., vol. 11, p. 095013, 2009.

[27] Berger, Claire, et al. “Electronic Confinement and Coherence in Patterned Epitaxial Graphene.” *Science*, vol. 312, no. 5777, 2006, pp. 1191–1196., https://doi.org/10.1126/science.1125925.

[28] Li, Xuesong, et al. “Large-Area Synthesis of High-Quality and Uniform Graphene Films on Copper Foils.” *Science*, vol. 324, no. 5932, 2009, pp. 1312–1314., https://doi.org/10.1126/science.1171245.

[29] Usui, Takane, et al. “Approaching the Limits of Dielectric Breakdown for SiO_2 Films Deposited by Plasma-Enhanced Atomic Layer Deposition.” *Acta Materialia*, vol. 61, no. 20, 2013, pp. 7660–7670., https://doi.org/10.1016/j.actamat.2013.09.003.

[30] Gomez-Diaz, J.S., et al. “Self-Biased Reconfigurable Graphene Stacks for Terahertz Plasmonics.” *Nature Communications*, vol. 6, no. 1, 2015, https://doi.org/10.1038/ncomms7334.

[31] Kroemer, H. Quasi-electric and quasi-magnetic fields in non-uniform semiconductors. *RCA Rev.* 18, 332–342 (1957).

[32] Dean, C. R. et al. Boron nitride substrates for high-quality graphene electronics. *Nat. Nanotechnol.* 5, 722–726 (2010).

[33] Zhong, Hua, et al. “Comparison of Mobility Extraction Methods Based on Field-Effect Measurements for Graphene.” *AIP Advances*, vol. 5, no. 5, 2015, p. 057136., https://doi.org/10.1063/1.4921400.

[34] Lee, Chang-Ju, et al. “Extraction of Intrinsic Field-Effect Mobility of Graphene Considering Effects of Gate-Bias-Induced Contact Modulation.” *Journal of Applied Physics*, vol. 127, no. 18, 2020, p. 185105., https://doi.org/10.1063/1.5128050.

[35] Kim, Seyoung, et al. “Realization of a High Mobility Dual-Gated Graphene Field-Effect Transistor with al2o3 Dielectric.” *Applied Physics Letters*, vol. 94, no. 6, 2009, p. 062107., https://doi.org/10.1063/1.3077021.

[36] K. I. Bolotin, K. J. Sikes, Z. Jiang, G. Fundenberg, J. Hone, P. Kim, and H. L. Stormer. “Ultrahigh Electron Mobility in Suspended Graphene.”. *Solid State Commun*. https://doi.org/10.1016/j.ssc.2008.02.024 146, 351 (2008).

[37] De Fazio, Domenico, et al. “High-Mobility, Wet-Transferred Graphene Grown by Chemical Vapor Deposition.” *ACS Nano*, vol. 13, no. 8, 2019, pp. 8926–8935., https://doi.org/10.1021/acsnano.9b02621.

[38] Wang, S, et al. “Photocurrent Generation of a Single-Gate Graphene p–n Junction Fabricated by Interfacial Modification.” *Nanotechnology*, vol. 26, no. 38, 2015, p. 385203., https://doi.org/10.1088/0957-4484/26/38/385203.

[39] Tan, Y.-W., et al. “Measurement of Scattering Rate and Minimum Conductivity in Graphene.” *Physical Review Letters*, vol. 99, no. 24, 2007, https://doi.org/10.1103/physrevlett.99.246803.

[40] Stanford Research Systems. (1993). *Model SR830 DSP Lockin-Amplifier Manual* https://www.thinksrs.com/downloads/pdfs/manuals/SR830m.pdf.

[41] Kobayashi, Shiho, et al. “Photoresponse of Graphene Field-Effect-Transistor with N-Type Si Depletion Layer Gate.” *Scientific Reports*, vol. 8, no. 1, 2018, https://doi.org/10.1038/s41598-018-22974-7.

[42] Mueller, T., Xia, F. & Avouris, P. Graphene photodetectors for high-speed optical communications. *Nature Photon* 4, 297–301 (2010). https://doi.org/10.1038/nphoton.2010.40

[43] Karch, J., et al. “Dynamic Hall Effect Driven by Circularly Polarized Light in a Graphene Layer.” *Physical Review Letters*, vol. 105, no. 22, 2010, https://doi.org/10.1103/physrevlett.105.227402.

[44] Sounas, Dimitrios, and Christophe Caloz. “Novel Electromagnetic Phenomena in Graphene and Subsequent Microwave Devices Enabled by Multi-Scale Metamaterials.” *Metamaterial*, 2012, https://doi.org/10.5772/37691.

[45] Christofi, Artisti, et al. “Giant Enhancement of Faraday Rotation Due to Electromagnetically Induced Transparency in All-Dielectric Magneto-Optical Metasurfaces.” Optics Letters, Optical Society of America, 11 Apr. 2018

[46] Orfanidis, Sophocles J. “5.4 Single Dielectric Slab.” *Electromagnetic Waves and Antennas*, Sophocles J. Orfanidis, New Brunswick, N.J.?, 2016.

[47] Dorney, Timothy D., et al. “Material Parameter Estimation with Terahertz Time-Domain Spectroscopy.” *Journal of the Optical Society of America A*, vol. 18, no. 7, 2001, p. 1562., https://doi.org/10.1364/josaa.18.001562.

[48] J. L. Tomaino, A. D. Jameson, J. W. Kevek, M. J. Paul, A. M. van der Zande, R. A. Barton, P. L. McEuen, E. D. Minot, and Y.-S. Lee, “Terahertz imaging and spectroscopy of large-area single-layer graphene,” Opt. Express 19(1), 141–146 (2011).

[49] Tonouchi, M. Cutting-edge terahertz technology. *Nature Photon* 1, 97–105 (2007). https://doi.org/10.1038/nphoton.2007.3

[50] Nagai, N., Kumazawa, R. & Fukasawa, R. Direct evidence of inter-molecular vibrations by THz spectroscopy. *Chem. Phys. Lett.* 413, 495–500 (2005).

[51] Taday, P. F., Bradley, I. V., Arnone, D. D. & Pepper, M. Using terahertz pulse spectroscopy to study the cryastalline structure of a drug: A case study of the polymorphs of ranitidine hydrochloride. *J. Pharm. Sci.* 92, 831–838 (2003).

[52] Woodward, R. M. et al. Terahertz pulse imaging in reflection geometry of human skin cancer and skin tissue. *Phys. Med. Biol.* 47, 3853–3863 (2002).

[53] Balos, Vasileios, et al. “Terahertz-Magnetic-Field Induced Ultrafast Faraday Rotation of Molecular Liquids.” *Physical Review Letters*, vol. 124, no. 9, 2020, https://doi.org/10.1103/physrevlett.124.093201.

[54] Heyman, J. N., et al. “Carrier Heating and Negative Photoconductivity in Graphene.” *Journal of Applied Physics*, vol. 117, no. 1, 2015, p. 015101., https://doi.org/10.1063/1.4905192.

[55] Heyman, J. N., et al. “Ultrafast Terahertz Faraday Rotation in Graphene.” *Journal of Applied Physics*, vol. 116, no. 21, 2014, p. 214302., https://doi.org/10.1063/1.4903212.

[56] Shi, S.-F., et al. “Controlling Graphene Ultrafast Hot Carrier Response from Metal-like to Semiconductor-like by Electrostatic Gating.” *Nano Letters*, vol. 14, no. 3, 2014, pp. 1578–1582., https://doi.org/10.1021/nl404826r.

[57] Candussio, S., et al. “Terahertz Radiation Induced Circular Hall Effect in Graphene.” *Physical Review B*, vol. 105, no. 15, 2022, https://doi.org/10.1103/physrevb.105.155416.

[58] “CVD Graphene: Single and Multiple Layers Graphene Supplier.” *ACS MATERIAL*, https://www.acsmaterial.com/materials/cvd-graphene.html.

[59] Reina, A. et al. Large area, few-layer graphene films on arbitrary substrates by chemical vapor deposition. *Nano Lett.* 9, 30–35 (2009).